Experimental Neurology 385 (2025) 115099

Contents lists available at ScienceDirect

Experimental Neurology

journal homepage: www.elsevier.com/locate/yexnr

Research paper

Early trigeminal and sensory impairment and lysosomal dysfunction in accurate models of Wolfram syndrome

Kerli Tulva [a,1,2], Aleksander Pirajev [a,2], Akbar Zeb [a,2,3], Asya E. Aksoy [a], Azizah Bello [a], Benjamin Lee [a], Baldvin F. Guðjónsson [a], Sigridur B. Helgadottir [a], Toomas Jagomäe [b,c], Andrea García-Llorca [d,4], Thor Eysteinsson [d], Monika Jürgenson [a], Mario Plaas [b,c], Eero Vasar [c], Allen Kaasik [a], Miriam A. Hickey [a,*]

[a] Department of Pharmacology, Institute of Biomedicine and Translational Medicine, University of Tartu, Ravila 19, 50411 Tartu, Estonia
[b] Laboratory Animal Centre, Institute of Biomedicine and Translational Medicine, University of Tartu, Ravila 14B, 50411 Tartu, Estonia
[c] Department of Physiology, Institute of Biomedicine and Translational Medicine, University of Tartu, Ravila 19, 50411 Tartu, Estonia
[d] Department of Physiology, Faculty of Medicine, University of Iceland, 101 Reykjavík, Iceland

ARTICLE INFO

Keywords:
Dorsal root ganglia
Inflammation
Lysosome
Magnetic resonance imaging
Sensory behaviour
Mitochondria
Trigeminus

ABSTRACT

Wolfram syndrome (WS) is a rare condition caused by homozygous or compound heterozygous mutations in the WFS1 gene primarily. It is diagnosed on the basis of early-onset diabetes mellitus and optic nerve atrophy. Patients complain of trigeminal-like migraines and show deficits in vibration sensation, but the underlying cause is unknown. Using accurate cell models and two separate, accurate rodent models of WS that show excellent face and construct validity, here we have examined trigeminus, sensation and sensory neuronal function in WS. Analysis of ex vivo and in vivo MRI sequences revealed profound trigeminal atrophy in each rodent model, a novel finding in WS. Optic nerve atrophy is a diagnostic sign in WS, and trigeminal atrophy occurred at the time of earliest loss of optic nerve volume. We also observed deficits in mechanical sensation in our mouse WS model, and pathological analysis revealed extensive inflammation in trigeminal sensory nucleus, both of which are novel findings in WS. Sensory neurons (dorsal root ganglia) showed impaired calcium handling upon depolarisation and reduced mitochondrial membrane potential. Finally, lysosomes were smaller, soma lysosome content was decreased and importantly, lysosome acidity was impaired in sensory neurons, all of which are novel findings in WS. We validated these findings using two separate publicly available datasets, both from WS patient fibroblast-derived neural stem cells. We observed a highly significant functional enrichment of GO cellular component lysosome-related terms among the differentially expressed proteins and genes, with the majority of lysosome-related proteins being downregulated. These data reveal extensive impairments in the trigeminal pathway and nociceptive neurons in WS that may contribute to trigeminal and sensory symptoms observed in patients. Moreover, we note that mutations in WFS1 are relatively common and, given the importance of WFS1 for sensory function, our data may also shed light on sensory impairments in general.

1. Introduction

Wolfram syndrome (WS) is a rare disorder diagnosed on the basis of early-onset non-autoimmune diabetes mellitus and optic atrophy(Rigoli et al., 2022). Over half of patients will develop diabetes insipidus and urinary tract deficits, and neurological deficits are also observed(de Heredia et al., 2013). Unfortunately, patients show a shortened lifespan with respiratory failure being the leading cause of death, typically

* Corresponding author at: Department of Pharmacology, Institute of Biomedicine and Translational Medicine, Faculty of Medicine, University of Tartu, Rm 3046 Ravila 19, Tartu, 50411, Estonia.
E-mail address: miriam.ann.hickey@ut.ee (M.A. Hickey).
[1] Present address: Department of Neurobiology, University of Osnabrück, Barbarastrasse 11, 49076 Osnabrück, Germany.
[2] Indicates equal contribution.
[3] Present address: Interchemie Company, Vanapere tee 14, Püünsi, 74013 Harju, Estonia.
[4] Present address: Department of Ophthalmology, University of California Davis, Davis, California, USA.

https://doi.org/10.1016/j.expneurol.2024.115099
Received 30 August 2024; Received in revised form 4 November 2024; Accepted 4 December 2024
Available online 9 December 2024

between the ages of 30 and 40 years(de Heredia et al., 2013).

We have previously reported that mice with Wfs1 deficiency show optic nerve atrophy(Cagalinec et al., 2016) and impaired glucose tolerance(Luuk et al., 2009), thus, this model shows both construct validity and face(Willner, 1984) validity. WS in humans is associated with greatly reduced volume of pons and cortex(Hershey et al., 2012; Lugar et al., 2019), and we have also reported these outcomes in these mice(Cagalinec et al., 2016). Furthermore, we have shown optic atrophy and brainstem atrophy, together with elevated blood glucose, in a rat model of WS(Plaas et al., 2017). These excellent animal models are therefore ideal for understanding phenotypes associated with this rare, complex syndrome.

WS is caused by homozygous or compound heterozygous mutations in the WFS1 gene primarily, including substitutions, frameshifts, nonsenses and deletions, and it is inherited in an autosomal recessive manner(Rigoli et al., 2022). WFS1 heterozygous mutations inherited in an autosomal dominant manner are also pathogenic and lead to low-frequency hearing loss(Lim et al., 2023) and cataracts(Berry et al., 2013; Krutish et al., 2023). Wolfram-like syndrome, also caused by mutations in WFS1, is an additional autosomal dominant condition that can cause hearing impairment(De Muijnck et al., 2023). However, WS patients show deficits in vibration sensation(Marshall et al., 2013), and smell identification and smell sensitivity deficits appear to progress with age(Alfaro et al., 2023, 2020). In addition, trigeminal neuralgia-like headaches are observed in WS patients(Stone et al., 2021; Urano, 2016) but the cause and underlying pathophysiology is unknown.

The trigeminus, or cranial nerve V, is a mixed sensory and motor nerve that mediates all sensory input from the face and controls some aspects of mastication in both humans(Standring, 2008) and mice (Fernández-Montoya et al., 2017; Vermeiren et al., 2020). Here, we report, for the first time, trigeminal atrophy in accurate rodent models of WS, which was accompanied by trigeminal sensory impairment in our mouse model of WS. Neuropathological analysis revealed that this atrophy and behavioural impairment was accompanied by extensive inflammation in trigeminal sensory nucleus (TSN). To examine sensory neurons specifically, we prepared primary DRG cultures and we report profound impairment of nociceptive neurons – reduced responsiveness to depolarising stimulation and impaired mitochondrial membrane potential – mirroring our previous findings from primary cortical neurons deficient in Wfs1(Cagalinec et al., 2016). Despite the mitochondrial impairment, we found no evidence of lysosomal biogenesis, and indeed, we observed a loss of functional (acidic) lysosomes. Finally, using publicly available proteomics data(Zmyslowska et al., 2021) and transcriptomics data(Pourtoy-Brasselet et al., 2021), we show an early enrichment of lysosomal GO cellular component terms within the differentially expressed proteins and genes, respectively, in neural stem cells derived from WS patient fibroblasts compared with healthy cells. In addition, the majority of lysosomal proteins were downregulated, corroborating our findings of extensive lysosomal impairment from an early disease stage in WS.

These data suggest that Wfs1 is critical for normal trigeminal and peripheral sensory nerve function and are in line with the impaired sensory function noted in patients with WS. These data show that lysosomal impairment is a very early feature of WS and that Wfs1 and WFS1 are essential for normal lysosomal function. Moreover, the prevalence of heterozygote carriers of WS is estimated to be 0.3–1 %(Aloi et al., 2012; Bespalova, 2001), thus, our data may also be relevant in the broader context of sensory impairment in the general population.

2. Methods

2.1. Mouse and rat husbandry and genotyping

We used a mouse model of WS on a B6N/129 mixed background in which more than 60 % of the total coding sequence of Wfs1 is deleted (Luuk et al., 2009); we refer to them as Wfs1 deficient mice. Heterozygous female and male Wfs1 deficient mice were bred to generate experimental groups of WT and homozygous-deficient mice for behaviour, imaging and pathology – hereafter referred to as WT and Wfs1 deficient. Male mice were used as their phenotype advances more quickly than female mice. WT × WT and homozygous Deficient × homozygous Deficient pairings were used to generate DRGs for in vitro experiments. Mixed sex pups were used at the ages of P5-P14.

Our rat model of WS has a deletion of exon 5; WT and homozygous deficient rats were used and we refer to them as WT and Wfs1 deficient rats (Plaas et al., 2017). All rodents were housed in temperature, humidity and light-controlled atmospheres. Authorisation was provided by the Estonian Animal Welfare authorisation committee, licence numbers 68, 90, 93, 94 and 203 according to the EU Directive 2010/63/EU. Animals were genotyped by PCR, as previously described(Luuk et al., 2008; Plaas et al., 2017). Our experiments were well powered and conform to ARRIVE guidelines(Percie du Sert et al., 2020) (supplementary file 1 Table S1).

2.2. Ex vivo magnetic resonance imaging

See Table 1 for details. MRI data from 1-year-old mice were from sequences that have been published previously. For data from in vivo imaging of live rats, datasets from(Plaas et al., 2017) were used.

Volumes were segmented manually by a blinded observer using ITK-SNAP (V3.8.0) and based upon Allen brain atlas for mice (https://mouse.brain-map.org/static/atlas) and the scalable MRI reference atlases for mice or for rats (https://scalablebrainatlas.incf.org/index.php).

For P10 and P22 analysis, total brain segmentation and trigeminal nerve segmentation began at the most rostral cortex, overlying the olfactory areas. Total brain segmentation ended with the last slice to contain both medulla and cerebellum. Trigeminal segmentation ended when there was bilateral contact between the trigeminae and the pons. Optic nerve segmentation began where the nerves exited the foramina and ended where they joined to form the chiasm. Due to reduced white matter content in these neonates, the optic chiasm and tract were not segmented and the optic nerve was not segmented from $N = 1$ WT mouse at P22.

Brain stem (pons and medulla) segmentation began at the most rostral portion of the pons, ventral to the interpeduncular nucleus and cerebellar peduncle, approximately bregma −3.6 mm in an adult mouse (equivalent for P10 and P22) and ended at the termination of the overlying cerebellum, approximately bregma −8.5 mm (equivalent for P10 and P22). Segmentation of thalamus began at the stria medullaris and continued until approximately −3.5 mm caudal to bregma when the medial geniculate complex could no longer be identified. For trigeminae in 8-m-old and 1-year-old mice, segmentation began from just after the end of the eyes and continued until bilateral contact was made with the pons. Volumes of cranial nerve II, brainstem, cortex and total brain from the 1-year-old mice have been published previously(Cagalinec et al.,

Table 1
T2 RARE sequences used for MR imaging.

Age	Sequence
P10 mice	Tr, 7600 ms; TE, 50.03 ms; imaging matrix, 320 × 320 × 50 (x,y,z); spatial resolution, 0.04688 × 0.04688 × 0.25 mm
P22 mice	Tr, 5256 ms; TE, 33 ms; imaging matrix, 320 × 320 × 50 (x,y,z); spatial resolution, 0.04688 × 0.04688 × 0.3 mm
8 m mice	Tr, 900 ms; TE, 47.13 ms; imaging matrix, 360 × 512 × 80 (x,y,z); spatial resolution, 0.0444 × 0.03 × 0.2 mm
1 yr mice[a]	Tr, 900 ms; TE, 47.13 ms; imaging matrix, 360 × 512 × 80 (x, y, z); spatial resolution, 0.0444 × 0.03 × 0.2 mm
17 m rats (ex vivo)	Tr, 900 ms; TE, 47.13 ms; imaging matrix, 320 × 320 × 160 (x, y, z); spatial resolution, 0.125 × 0.125 × 0.25 mm
15 m rats (in vivo)[b]	Tr, 6803 ms; TE, 33 ms; imaging matrix, 320 × 320 × 65 (x, y, z); spatial resolution, 0.1562 × 0.1562 × 0.5 mm

[a] Image series from (Cagalinec et al., 2016).
[b] Image series originally from (Plaas et al., 2017).

2016).

For rats, total brain was segmented from after the end of eyes and finished with the last slice that contained cerebellum. For ex vivo sequences, trigeminae were segmented from the level where the eyes ended, until bilateral contact with the pons. In vivo imaging was of lower resolution due to the shorter imaging time, and trigeminae were segmented from eruption from foramina until bilateral contact with the pons.

2.3. Pathological analysis

Brains (1 hemisphere per mouse) and trigeminae were prepared for cryosectioning as previously described(Faisal et al., 2023) and group sizes were based upon our previous sample size calculations where there were also large differences in GFAP and in IBA1 between genotypes (Faisal et al., 2023). Mice were 8 months of age, male, and group sizes were $N = 3$ WT, N = 3 Wfs1 deficient, with two technical replicates (two cryosections) per mouse for each antigen or stain. For demonstration of trigeminal motor and sensory nucleus, sections from WT mice were stained for cresyl violet. Directly adjacent sections were stained for Wfs1. Additional cryosections (WT only; approx. −1.7 mm from bregma) were used to provide positive controls for Wfs1 in hippocampus CA1 and cortical layer II. Cryosections of trigeminus itself were also examined for Wfs1 in WT mice. For Wfs1 staining, sections were incubated in fresh TE antigen retrieval solution as per manufacturer's instructions and then incubated in rabbit polyclonal anti-Wfs1 (1:400, Proteintech Cat# 26995–1-AP, RRID:AB_2880717) overnight, followed by washing (3 × 5 min) and incubation with secondary antibody (Jackson Immuno goat anti-rabbit 1:200; 2 h at room temperature). For GFAP and IBA1 staining in WT and Wfs1 deficient mice, sections at the level of −5.3 mm from bregma were washed, blocked, and then incubated with anti-GFAP (1:1000, Atlas Antibodies Cat# HPA056030, RRID:AB_2683015) or anti-IBA1 (1:500, Abcam Cat# ab5076, RRID: AB_2224402), as we have previously shown(Faisal et al., 2024, 2023), for 3 days and then washed (3 × 5 min), incubated with secondary antibodies (Jackson Immuno goat anti-rabbit or rabbit anti-goat, respectively, 1:200; 2 h at room temperature), stained with Hoechst and then mounted on gelatin-coated slides.

Images of cresyl violet-stained sections were taken using PlanNeo-Fluar Z 1.0× objective, at 30× magnification (effective NA 0.25) using an AxioCam HR R3 camera on a Zeiss Observer stereomicroscope. Following counterstaining with Hoechst and mounting, images of Wfs1 staining were taken using an LSM 780 confocal using Plan Apochromat ×20/0.8 objective (425.1 × 425.1 μm, 1024 × 1024 pixels; ex/em: Wfs1 561 nm 585-733 nm, 1 AU; ex/em: Hoechst 405 nm/410-579 nm 1.3 AU). For GFAP, photomicrographs through the section thickness were taken using Zen software (Plan-Apochromat 10×/0.45 M27 objective) on a Zeiss LSM780 confocal microscope (1.38 × 1.38 × 4.13 μm; 1024 × 1024; ex/em GFAP 561 nm/585-733 nm 1.36 AU; ex/em Hoechst 405 nm/414-552 nm 1.86 AU). ImageJ was used to separate the channels, make Z projections, and auto-threshold. Regions of interest were drawn based upon Hoechst channel and the mean gray value of the RoIs in the GFAP channel quantified. For IBA1, photomicrographs through the section thickness were taken using Zen software (Plan-Apochromat ×40/1.3 oil DIC M37 objective; Airy unit 1; 0.21 × 0.21 × 0.55 μm; 1024 × 1024, ex/em: 561 nm/585-733 nm) on an LSM780 Zeiss confocal microscope ($N = 3$ images per section). ImageJ was used to separate the channels, make Z projections, and for auto-thresholding. The Remove Outlier and Despeckle functions were then used. Particles greater than 30μm^2 were quantified and the mean particle size per mouse used for comparisons. We have previously validated this method for quantifying activated microglia, using the well-established 5xFAD mouse model of Alzheimer's disease(Faisal et al., 2023). Control sections incubated without primary antibody were included within each experiment, and no specific staining was observed. Exclusion criteria: none, all data were used for analysis.

2.4. Behavioural testing

Trigeminal function was tested by quantifying response to von Frey hairs of increasing weight applied to the muzzle, as described previously (Krzyzanowska et al., 2011) (males; 8 months; total number was 7–8, total number in each task was 7–8, no exclusion criteria – all data were included(Percie du Sert et al., 2020)). The response to an air puff from a plastic Pasteur pipette to the side of the head (normal response or poor response; poor response = no blink and/or slow blink) was also examined. Body weight was recorded regularly. Climbing(Hickey et al., 2008, 2005) and grip strength(Faisal et al., 2024) were tested as described previously. Exclusion criteria: none, all data were used for analysis.

2.5. Semi-thin section preparation

Semi-thin sections from a group of 4 WT and 6 Wfs1 deficient mice (8 months of age) were prepared by the Transmission electron microscopy (TEM) laboratory, Institute of Molecular and Cell Biology, of the University of Tartu. Three photomicrographs of each of 5–6 trigeminal sections per mouse were taken at 63× magnification using Stereo-investigator (V5, Microbrightfield, US) using a Zeiss Observer Z1 microscope. Using ImageJ batch processing, images were thresholded and the Analyse particle function was used to quantify axon size (within myelin sheaths).

2.6. qPCR

Mice (male; P22, WT $N = 5$, Wfs1 deficient N = 5; 8 m WT $N = 7$, Wfs1 deficient $N = 6$) were euthanised by cervical dislocation followed by decapitation and trigeminal tissue snap-frozen in liquid nitrogen within approximately 2–3 min and subsequently stored at −80 °C. Total RNA was purified using Qiagen RNeasy® Mini Kit (Qiagen), integrity checked using Agilent RNA 6000 Nano Kit on a bioanalyzer (Agilent, 2100) and then stored at −80 °C. cDNA was synthesised using the SuperScript III RT Kit (Invitrogen, cat. no. 18080–044) and then stored at −80 °C. The cDNA was then used for quantitative real-time PCR on QuantStudio 12 K Flex instrument from Applied Biosystems (in-house). PCRs were performed using Fast SYBR Green Master Mix (Life Sciences, cat. no. K0229). Each assay included: 1) a standard curve of five serial dilution points of control cDNA (mouse EST clone of appropriate fragment of the gene of interest (Invitrogen, CA), 2) sample cDNA, 3) no template control, 4) no reverse transcriptase control. All samples were run in triplicates. The PCR cycling parameters were: 95 °C for 5 min (1 cyc); 95 °C for 10 s, 65 °C for 10 s, 72 °C for 10 s (40 cyc). A dissociation protocol was established at the end of each run to verify the presence of a single product. The relative expression of genes of interest was normalised to HPRT and actin, which were run in parallel, and was calculated from Ct values using the $2^{-\Delta\Delta Ct}$ method(Schmittgen and Livak, 2008). For primers (Tag Copenhagen, Frederiksberg, Denmark), see Table 2. Our qPCR followed MIQE guidelines(Bustin et al., 2009).

2.7. Cell culture

2.7.1. Isolation and culturing

Mixed-sex pups, aged P5-P14, were euthanised by decapitation and dorsal root ganglia (DRGs) isolated and placed in ice-cold sterile PBS. DRGs were transferred to a dissociation solution (2 mg/ml collagenase, + 0.1 mg/ml DNase; Gibco) and incubated for 40 min at 37 °C. Cells were then incubated in trypsin (0.025 %) for an additional 5 min at 37 °C and then in DMEM/F-12 + 10 % foetal bovine serum (SigmaAldrich) to quench trypsinization. Cells were then triturated, centrifuged (10 min at 600*g*) and the resulting pellet was resuspended in fresh complete medium. An equivalent of 2 ganglia per 50 μl were plated per quadrant of 4-quadrant dishes (Cell Vis 4-chamber glass-bottom dishes; Gerasdorf Austria) or 8 ganglia per 200ul per 35-mm glass-bottomed dish (MatTek, MA). Coverslips were coated with laminin and PDL. After 3–4 h at 37 °C

Table 2
Primers used for qPCR.

qPCR primers	
HPRT	F: GCA GTA CAG CCC CAA AAT GG R: CAA GGG CAT ATC CAA CAA CA
Beta-Actin	F: ATG GTG GGA ATG GGT CAG AAG R: TCT CCA TGT CGT CCC AGT TG
Wfs1	F: ACT ACC TAC GCC TTG CCA AC R: CCA GTA CAT GAC CAG GGC AG
Beclin1	F: GAA ACT GGA CAC GAG CTT CA R: CAT CCT GGC GAG TTT CAA TA
P62	F: GAT GGG GAC TTG GTT GCC TT R: TTG CTG TGT TCC CTG TGC AG
LC3a	F: AGG AAT GTT GTG ACC TGA CGT R: TCT GCT GCA CCT CCT TAC AG
Bnip3	F: ATG GCA ATG GGA GCA GCG TT R: TAT CTT GTG GTG TCT GGG AG
Park2	F: GGT TTC TGA GGG CTT CAC AG R: TCA ACC TTC CAG GCA ATT TT
TrpM8	F: ATA GGC GAG GTG GTG AGA GA R: GGT GGG TAT GGT TGT TGT CC
TrpA1	F: TCC ACG TGT GCC AAA GAC AA R: CCC TGC TGT AGC CGT TCT TT

and 5 % CO_2, cells were supplemented with complete medium (Neurobasal A (ThermoFisher), B27 supplement (ThermoFisher), Gentamicin and glutaMAX (Thermofisher)). The following day, medium was replaced with fresh medium containing 1.5 μM cytarabine (SigmaAldrich) to reduce proliferation of fibroblasts. WT and Wfs1 deficient neurons were always prepared, cultured and imaged in parallel.

2.7.2. Calcium transients

Cells aged 3–4 weeks were used. Medium was removed, and cells were incubated for 30 min in warmed Krebs containing 5 μM Fluo-4 (ThermoFisher, prepared with pluronic 4 %), washed and then imaged in warmed Krebs using an LSM 780 confocal microscope at 37 °C. Images were taken every 2.5 s for approximately 7 m. The initial two minutes were used for baseline, and 40 mM KCl was added at approximately 120 s to induce calcium transients. Imaging specifications were as follows: objective, Plan-Apochromat 20×/0.8; ex: 488 nm; em 499-568 nm; pixel size: 0.69 × 0.69 × 1 μm; pixel time 3.15 μs; FOV:708.49 μm^2. After the time series, a Z stack of the field of view was taken for additional morphological confirmation that the signals were coming from DRGs, which sit on top of the layer of fibroblasts (cultures were treated with AraC but were considered mixed as some fibroblasts remained). For analysis, a region-of-interest for each DRG soma per field of view was generated in Zen software, which then created a table of fluorescence intensity over time. Transients that lasted less than 60s were removed, and transients from over-exposed cells were not analysed. The mean fluorescence during baseline was calculated from the table, and every timepoint was then expressed as a proportion of that baseline. Four separate experiments were conducted, WT $N = 234$ from 17 dishes, Wfs1 deficient $N = 177$ from 15 dishes, which were grouped together for analysis.

2.7.3. Mitochondrial membrane potential

Medium was removed from 3-week-old DRGs and replaced with medium containing TMRM (Tetramethylrhodamine methyl ester I34361 Thermofisher) at a final concentration of 10 nM (non-quenching (Connolly et al., 2018; Perry et al., 2011)). Cells were then placed back into the incubator for 30 min. Single-plane images of the soma were then taken using an LSM 780 confocal microscope at 37 °C (ex/em 561 nm/566-669 nm, 40×/1.3 oil DIC M27, 0.05 μm × 0.05 μm pixel size, 1024 × 1024 frame). For analysis, the soma was outlined. Only DRG soma with outlines fully contained with the field of view were analysed. The integrated fluorescence density and fluorescence intensity was measured from 16-bit images using ImageJ (FIJI). Four separate experiments were conducted, $N = 283$ WT DRGs (from 11 quadrants) and $N = 244$ Wfs1 deficient DRGs (from 10 quadrants), which were grouped together for analysis.

2.7.4. Lysosome quantification

Cells aged 3–4 weeks were used for imaging. Medium was removed and replaced with medium containing Lysotracker red (100 nM, L7528 Thermofisher) and CellTracker green (6 μM, C7025, Thermofisher). Cells were incubated in the dark, at 37 °C, for 1 h, washed gently and imaged in warmed Krebs. A 10-μm stack through the middle of each DRG soma, identified based upon CellTracker, was taken using an LSM780 confocal LCI Plan-Neofluar 63×/1.3 Imm Korr DIC M27 (pixel size 0.7 μm × 0.7 μm × 0.397 μm). Excitation and emission were 561 nm (LysoTracker) and 488 nm (CellTracker), and LP575nm and BP 505-550 nm, respectively. Only DRG soma with outlines fully contained with the field of view were analysed. For analysis in Fiji (ImageJ), image stacks from the fields of view were cropped to the soma size based upon CellTracker staining. The red channel was then despeckled and thresholded and then individual lysosomes quantified using the 3D objects counter. Four separate experiments were conducted, $N = 149$ WT DRGs (14 quadrants) and $N = 143$ Wfs1 deficient DRGs (14 quadrants), which were grouped together for analysis.

2.7.5. Quantification of lysosome acidity

Cells aged 3–4 weeks were used. Medium was removed and cells were treated with medium containing 100 nM Lysotracker red for 55 min in the dark, then Lysosensor (LysoSensorGreen DND-189) added for a final concentration of 1 μM. At 60mins, the medium was removed, the cells washed in warmed Krebs and then imaged in warmed Krebs. Images were taken at ×63 (1.4 oil DIC M27) using "line" scan such that Lysosensor and Lysotracker were excited at the same time at 405 nm and 561 nm, respectively (512 × 512 pixels, 33.74 × 33.74 μm so that for each pixel the dimensions were XY 0.07 × 0.07 μm with a Z step of 0.34 μm). Emissions were collected at 410-556 nm (Lysosensor) and 566-691 nm (Lysotracker). Images were analysed using ImageJ macros; briefly, images were split into red and green channels, and a z-stack from 10 sequential optical sections retained for analysis. The soma was then outlined (faintly shown by Lysosensor). Only DRG soma where outlines were fully contained with the field of view were analysed. For each channel, the background was subtracted using a rolling ball radius of 25 pixels, and images were then auto-thresholded and despeckled. Resulting particles within the soma, for each optical section of the stack, were added to the RoI manager. The proportion of Lysosensor-positive staining that was contained within Lysotracker particles, per optical slice, was then quantified and an average per cell calculated. Four separate experiments were conducted ($N = 206$ WT DRGs from 15 quadrants, $N = 210$ Wfs1 deficient DRGs from 12 quadrants).

2.8. Analysis of proteomics and transcriptomics from publicly available datasets

Open source proteomics data from $N = 3$ healthy and $N = 3$ WS fibroblast-derived untreated neural stem cell samples were obtained from(Zmyslowska et al., 2021). For initial analysis, expression levels of lysosomal matrix proteins ($N = 63$(Schröder et al., 2010)) that were expressed by the cells ($N = 45$) and lysosomal integral membrane proteins or protein complexes of the lysosome membrane ($N = 45$) that were expressed by the cells ($N = 21$) were extracted and placed into Morpheus (https://software.broadinstitute.org/morpheus) for visual representation.

Separately, the untreated healthy and WS human neural stem cell proteomic dataset was compared using the False Discovery rate approach (Two-stage step-up method of Benjamini, Krieger and Yekutieli; desired FDR (q) = 5 %). Of the 8047 proteins in the dataset, 3308 were expressed differentially (q value 0.05 or less). Functional enrichment analysis was performed on these 3308 proteins using g:Profiler (version e111_eg58_p18_f463989d) with g:SCS multiple testing correction method applying significance threshold of 0.05(Kolberg et al., 2023) and with DAVID Bioinformatics(Huang et al., 2009; Sherman et al., 2022). Gene ontology cell component (GO CC) terms primary lysosome (GO:0005766), lysosome (GO:0005764) and lysosomal lumen (GO:0043202) were examined. Finally, the hits identified by DAVID, from the proteomics dataset(Zmyslowska et al., 2021), were then inputted onto lysosome KEGG pathway 04142 ("lysosome") to provide a visual representation of the dysregulated lysosome proteins.

We also examined transcriptomics data from N = 3 healthy and N = 3 WS undifferentiated and differentiated fibroblast-derived neural stem cells from(Pourtoy-Brasselet et al., 2021). Based upon the published padj values, the 8786 genes that were differentially expressed were examined using G:Profiler and DAVID for GO CC.

2.9. Statistical analyses

All analyses were conducted blinded, prior to graphing and statistical analysis. Individual data points with mean values ± standard error of the mean or 95 % confidence intervals are provided for optimal interpretation of robustness and effect sizes(du Sert et al., 2020; Dziak et al., 2020; Greenland et al., 2016; Heckman et al., 2022). The critical value was set to 0.05. To compare one factor between two separate groups, unpaired *t*-tests or Mann-Whitney tests were used. Unpaired *t*-tests were used when data had similar variances based upon F tests. Mann Whitney *U* tests were used where data were non-parametric, based upon F tests for variance and/or D'Agostino & Pearson and Kolmogorov-Smirnov tests for normality. Normality testing was used with large group sizes only, i.e., data from in vitro analyses where $N > 140$. Two-way ANOVAs (two-way or mixed effects) followed by appropriate post-hoc tests were used to compare data where there were two factors. Chi-square tests were used to compare trigeminal sensory function. For analysis of slopes of increase and decline of Fluo-4 relative fluorescence intensity, linear regressions were run. Data were fit to either straight line or to centred second-order polynomials (quadratic) based upon non-linear regression comparison of fits. AUC analyses were conducted to determine peaks of calcium transients. Linear regressions were also used to correlate blood glucose with volumetric data. GraphPad Prism V10.2.3 was used for statistical analyses. For analysis of effect sizes, G*Power was used (3.1.9.4). G*Power was also used to calculate sample sizes (Supplementary file 1, Table S1) except in the case of repeated categorical data

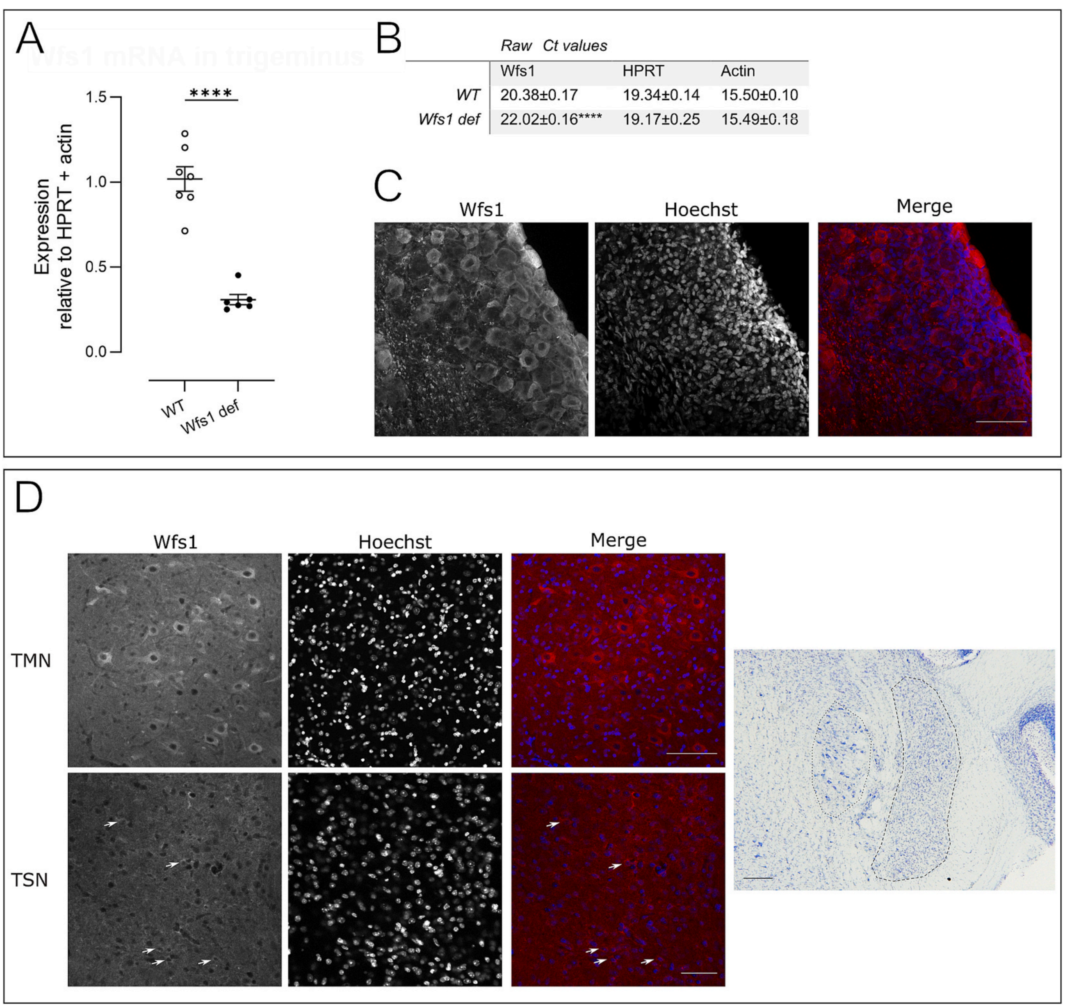

Fig. 1. A) Graph shows Wfs1 mRNA expression in WT and Wfs1 deficient trigeminus from 8 m old male mice, normalised to HPRT and actin using the $2^{-\Delta\Delta Ct}$ method. ****$p < 0.0001$ B) The table shows raw Ct values (mean ± sem). C) Wfs1 expression in normal mouse trigeminus. Scalebar = 100 μm. D) Wfs1 expression in the mouse TMN (top row), note the typically large soma of the neurons in this small nucleus. Scalebar = 100 μm. The second row shows Wfs1 staining in the mouse TSN, note, these images are zoomed-in slightly to depict the smaller neurons in this nucleus. Positively stained cells are shown by the arrows. Scalebar = 50 μm. For all confocal images, Wfs1 staining is shown in the left column, nuclear staining using Hoechst is shown in the middle column and the merged images are shown in the right column. Photomicrographs are not modified except for brightness and contrast. The cresyl violet-stained section shown on the right, D), shows the TMN (dotted line) and TSN (dashed line) (scalebar = 200 μm). TMN, trigeminal motor nucleus; TSN, trigeminal sensory nucleus. (For interpretation of the references to colour in this figure legend, the reader is referred to the web version of this article.)

(trigeminal von Frey sensation) where Glimmpse(Kreidler et al., 2013) was used. Statistical analysis of proteomics data is described above. Analysis of functional enrichments within the differentially expressed proteins or genes is described above.

3. Results

3.1. Wfs1 is highly expressed in trigeminal pathways

Importantly, we show that Wfs1 mRNA (Fig. 1A, B) and protein (Fig. 1C) are heavily expressed within the trigeminal tract and in neuronal soma of the trigeminal motor and sensory nuclei (Fig. 1D top row, Fig. 1D second row, respectively). To confirm the specificity of our antibody, in Fig. S1, we show positive staining in hippocampus CA1, which is well known for expression of Wfs1 (Luuk et al., 2008) and a clear lack of staining in CA1 when sections were not exposed to primary antibody. We also show positive staining for Wfs1 in cortical layer II, which is again well known for Wfs1 expression(Luuk et al., 2008). Thus, Wfs1 is heavily expressed in trigeminus and, as expected(Luuk et al., 2008), in second-order neurons of the trigeminal sensory pathway.

Patients show partial expression of the Wfs1 gene and protein(Hu et al., 2022; Philbrook et al., 2005). We note that the mice we use to model WS have had more than 60 % of their total Wfs1 coding sequence deleted(Luuk et al., 2009); we therefore call them Wfs1 deficient mice. In line with this, our Wfs1 deficient mice show much reduced expression of the gene in the trigeminus (Fig. 1A $2^{-\Delta\Delta Ct}$ comparison: $t = 8.5$, df = 11, $p < 0.0001$; Fig. 1B Raw Ct comparison: gene × genotype interaction: F(2,22) = 76.6, p < 0.0001).

3.2. Progressive brain volume changes in Wfs1 deficient mice that mirror changes in humans with Wolfram syndrome

Patients with WS show early changes in pons volume(Hershey et al., 2012; Lugar et al., 2019), and we therefore examined brain development in our Wfs1 deficient mice. We imaged mice at 10 days of age (P10) and at 22 days of age (P22), ex vivo. We examined volumes at each age: No difference in volume of total brain (Fig. 2A), optic nerve (Fig. 2C), brain stem (Fig. 2E) or cerebellum (Fig. 2G) was observed at either age. No difference was detected in body weight at these ages (P10 $t = 0.06$, df = 4, ns; P22 $t = 1.5$, df = 6, ns). Thus, these data reveal no gross abnormalities in brain development at the very earliest stages of WS. Data from P10 and P22 mice are combined for simplicity in Fig. 2 (A, C, E, G; triangles show P10 and circles show P22 mice; A: P10: $t = 0.2$, df = 4, ns; P22: $t = 0.1$, df = 6 ns; C: P10: $t = 0.3$, df = 3, ns; P22: t = 0.2, df = 6, ns. E: P10: $t = 0.6$, df = 4, ns, P22 t = 0.6, df = 6, ns. G: t = 0.2, df = 4, ns, P22 mice t = 0.6, df = 6, ns). We also analysed P10 and P22 data using ANOVA but again, we observed no difference in any of the segmented regions, at either age (genotype x age F (1, 4) = 0.2, ns; effect of genotype F (1, 4) = 0.0005, ns).

Previously, we showed reduced volume of the brainstem and optic nerve in 1-year-old male Wfs1 deficient mice(Cagalinec et al., 2016). We now reveal that total brain (Fig. 2B), cranial nerve II (Fig. 2D, optic nerve + chiasm + tract) and cerebellar volume (Fig. 2H) are reduced already at 8 months of age (see Table 3 for effect sizes and CI). We did not detect a difference in thalamic volume (Table 3). Thus, coupled with our previous demonstration of increased blood glucose(Luuk et al., 2009) in these mice, our data further demonstrate the excellent face validity of this mouse model, with progressive atrophy in clinically relevant areas of brain.

3.3. Progressive volume changes in trigeminus in Wfs1 deficient mice

We then examined the trigeminus in our ex vivo MRI sequences. No change in trigeminal volume was noted in P10 or P22 neonate mice, again suggesting no gross abnormalities in brain development (P10: $t = 0.5$, df = 4 ns; P22 t = 0.2, df = 6 ns). Data are shown together for simplicity (Fig. 3A). Although there was no change in total trigeminal volume (Fig. 3C), trigeminal atrophy began at 8 months of age in Wfs1 deficient mice, with the greatest effect observed caudally (Fig. 3 C, $t = 1.9$, df = 13, ns; Fig. 3 D: slice x genotype interaction F (39, 492) = 2.6, $p < 0.0001$). By 1 year, atrophy was extensive throughout the nerve, demonstrating progressive degeneration (Fig. 3 E: $t = 4.5$, df = 6, $p < 0.01$; Fig. 3 F: slice x genotype interaction F (39, 231) = 2.1, $p < 0.001$;) and causing a very large effect size (3.1; 95 % CI WT 9.3–11.2, 95 % CI for Wfs1 deficient 8.6–10).

Linear regressions showed that trigeminal and optic nerve volume never correlated with blood glucose levels (supplementary file 1 Table S1). This mirrors findings from patients, which showed that retinal thickness(Zmyslowska et al., 2017), smell deficits(Alfaro et al., 2020) and brain stem volume reduction(Lugar et al., 2019) are not a consequence of raised blood glucose per se. When comparing all total volumes at 8 months of age, total brain volume survived multiple comparisons (Table 3; region x genotype F(5, 65) = 10.6, $p < 0.0001$) and there was a strong overall effect of genotype (F (1,13) = 14.4, $p < 0.01$).

3.4. Volume changes in trigeminus in Wfs1 deficient rats

Given that trigeminal atrophy is a new phenotype of WS, we asked whether our rat model showed similar changes. First, we extended(Plaas et al., 2017) the face validity of this model. We observed reduced total brain volume, whether from ex vivo (17 months, $t = 3.1$, df = 6, $p < 0.03$, Fig. S2A) or in vivo (15 months, U (58,33) = 5, p < 0.03, Fig. S2C) sequences. Cerebellar gray matter was also reduced although there was no change in cerebellar white matter in the small group that we examined ex vivo (Fig. S2B; cerebellar white and gray matter, effect of subregion, F (1, 6) = 1621, $p < 0.0001$).

Having extended face validity, we then examined trigeminal volume. Importantly, we observed reduced volume in the Wfs1-deficient rats imaged ex vivo, again, at more caudal regions (Fig. 4 A: slice x genotype: F (69, 408) = 2.9, p < 0.0001). Total trigeminal volume was also reduced in these rats, with a large effect size (Fig. 4 B: $t = 2.7$, df = 6 $p < 0.04$, effect size 1.93; 95 % CI WT: 74.31–92.68; 95 % CI for Wfs1 deficient: 65.51–80.69). Trigeminal volume was also reduced a separate cohort of rats that we imaged in vivo (Fig. 4 C, effect of genotype: F (1,11) = 12.5, $p < 0.01$; Fig. 4 D; total volume: t-test, $t = 4.2$, df = 11 p < 0.01), and again, with a large effect size of 2.3 (95 % CI WT: 24–29.8; 95 % CI for Wfs1 deficient: 20.3–23.2).

Thus, our finding of trigeminal atrophy is reproducible in separate, validated rodent models of WS whether imaged using high resolution or low resolution relevant for imaging in live rats.

3.5. Functional deficits in trigeminal pathways in an accurate rodent model of WS

We examined behavioural sensory function in our 8-month-old WS mice, prior to MRI volumetric analyses. At this age, these mice show reduced weight (Fig. S3A, age x genotype interaction: F(21, 273) = 38.2, $p < 0.0001$), mildly reduced grip strength and reduced rearing exploration (Fig. S3 B, effect of genotype on grip strength F(1,13) = 15.8, p < 0.01; C, effect of genotype on climbing and rearing, F(1, 13) = 20.3, $p < 0.001$).

We examined trigeminal function using two separate tasks. Eyeblink involves the trigeminal V1 afferent branch, and slow reflex eye blinks are typical of an impaired trigeminal response(Lee et al., 2011). Wfs1 deficient mice showed an absent or slow response to an air puff to the eye (Fig. 5A, $X^2(69.5, 1)$, p < 0.0001). We also tested the mice using a validated test for trigeminal function(Krzyzanowska et al., 2011) based upon touch sensation via the V2 branch of the trigeminus. The Wfs1 deficient mice required larger von Frey hairs to instigate a response (Fig. 5B, $X^2(31.8, 5)$, $p < 0.0001$). Thus, our mice show reduced trigeminal sensation in two separate behavioural tests, at an age where earliest trigeminal atrophy is observed.

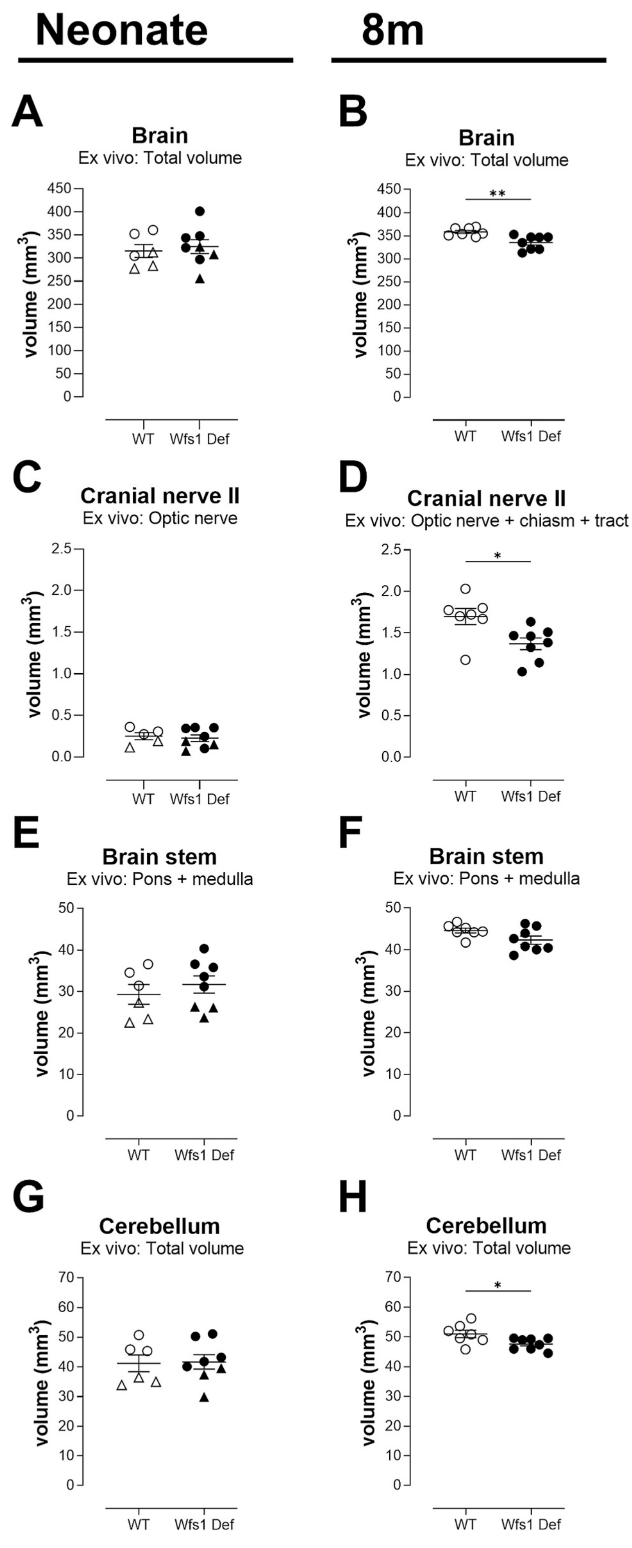

Fig. 2. Ex-vivo volumetric segmentation of perfusion-fixed brains from WT and Wfs1 deficient male mouse littermates. A) Volumes of total brain of mice aged 10 days (open or closed triangles) or 22 days (P22, open or closed circles). *t*-tests, P10: $t = 0.2$, df = 4, p = ns; P22: $t = 0.1$, df = 6 p = ns. B) Volumes of total brain of mice aged 8 months (8 m). By 8 m of age, Wfs1 deficient mice show reduced total brain volume ($t = 3.5$, df = 13, $^{**}p < 0.01$). C) Volumes of optic nerve in mice aged 10 days (P10, open or closed triangles) or 22 days (P22, open or closed circles). *t*-tests P10: $t = 0.3$, df = 3, p = ns; P22: t = 0.2, df = 6, p = ns. D) Volumes of optic nerve + optic chiasm + optic tract in mice aged 8 m. By 8 m, Wfs1 deficient mice show reduced volume ($t = 2.8$, df = 13, $^{*}p < 0.05$). E) Brainstem volume in P10 (triangles) or P22 (circles) mice. P10: $t = 0.6$, df = 4, ns. P22 t = 0.6, df = 6, p = ns. F) Brainstem volume in mice aged 8 m ($t = 1.9$, df = 13, ns). No differences in total volume were detected between the genotypes at 8 m. G) Cerebellar volume in P10 (triangles; t = 0.2, df = 4, ns) and P22 mice (circles; t = 0.6, df = 6, ns). H) Cerebellar volume in 8 m-old Wfs1 deficient mice. By this age, Wfs1 deficient mice showed reduced total cerebellar volume ($t = 2.4$, df = 13 $^{*}p < 0.05$). Symbols show data from individual mice with lines indicating mean ± sem. Asterisks show differences between genotypes.

Table 3
Brain volumetric analysis of 8-month-old WT and Wfs1 deficient male mice.

	WT			Wfs1 deficient			95 % CI	95 % CI	Effect size	P value[a]	P value[b]
Total volumes	Mean	SD	N	Mean	SD	N	WT (low-high)	Wfs1 deficient (low-high)			
Brain	358.3	8.8	7	335.4	15.3	8	350.2–366.4	322.7–348.2	1.84	p < 0.01	p < 0.03
Optic nerve	1.7	0.3	7	1.4	0.2	8	1.5–1.9	1.2–1.5	1.42	p < 0.02	
Trigeminus	10.3	1.0	7	9.3	0.9	8	9.3–11.2	8.6–10.0		ns	
Brainstem	44.6	1.6	7	42.3	2.8	8	43.2–46.0	40.0–44.7		ns	
Cerebellum	51.0	3.4	7	47.6	2.0	8	47.9–54.1	46.0–49.3	1.22	p < 0.04	
Thalamus	15.7	1.0	7	14.8	0.8	8	14.8–16.6	14.1–15.4		ns	

[a] Comparisons of individual regions.
[b] Post-hoc test results, following an ANOVA covering all regions – only statistically significant differences are shown.

3.6. Pathological changes in trigeminal system

Given the profound and progressive atrophy in trigeminus that we observed, and the deficits in behavioural response to trigeminal stimulation, we asked whether pathological changes occurred on a microscopic scale. When we examined 8-month-old WT and Wfs1 deficient mice, as expected, white matter tracts surrounding the TSN contained GFAP-positive astrocytes (e.g., the spinal tract of the trigeminal nerve, see Fig. 6). In TSN in WT mice, astrocytes were either absent, or at most, only one or two were present (Fig. 6, GFAP). However, in Wfs1 deficient mice, there was extensive infiltration of GFAP-positive astrocytes (3 out of 3 mice; $t = 13.27$, df = 4, $p < 0.001$), resulting in an extremely strong statistical effect size (effect size 10.8) and no overlap in 95 % confidence intervals between WT and WS mice (WT 95 % CI -1.2–3.3, Wfs1 deficient 95 % CI 15.4–27.98). With regard to microglia, IBA1-stained microglia were more activated in TSN in Wfs1 deficient mice because they were larger and "bushier" when compared with microglia that are normally present in TSN in WT mice (Fig. 6, IBA1; $t = 5.2$, df = 4, p < 0.01). This effect was also very strong (effect size = 4.2) with very little overlap in the 95 % confidence intervals (WT 95 % CI 108.3–177.1, Wfs1 deficient 95 % CI 166.0–279.4). Thus, behavioural sensory impairments and trigeminal atrophy in our accurate rodent models are accompanied by extensive inflammation of the TSN.

When we analysed the morphology of caudal trigeminus in semi-thin sections from a separate group of 8-month-old mice, Wfs1 deficient axons were smaller, as demonstrated by cumulative frequency distribution of axon area (supplemental file 1, Fig. S4 A, genotype x area size interaction: F(100, 13,200) = 3.1, $p < 0.0001$; Fig. S4 B mean axon area per field of view, t(132) = 3.7, $p < 0.001$), although this difference did not reach significance when mean axon area per mouse was used (Fig. S4C, $t = 2$, df = 8, $p = 0.086$).

3.7. Sensory neurons show reduced calcium transients and impaired mitochondria

We have previously shown altered calcium responses and reduced membrane potential in normal primary cortical neurons depleted of Wfs1, which led to alterations in mitochondrial dynamics(Cagalinec et al., 2016). We therefore asked if sensory neurons showed similar changes. We used dorsal root ganglia (DRGs) to increase our population of sensory neurons. Peak calcium transients were reduced in mature (3–4-week-old) sensory neurons from Wfs1 deficient mice (Fig. 7 A: time x genotype F(156, 63,335) = 13.30, p < 0.0001; Fig. 7 D: Mann-Whitney test p < 0.0001, U = 14,595, effect size = 0.61 (medium); WT 95 % CI = 1.7–1.9, Wfs1 deficient 95 % CI = 1.5–1.6). Moreover, the rate of rise in intracellular calcium and the rate of decline/recovery were both reduced in sensory neurons from Wfs1 deficient mice (rise: Fig. 7 B, slope of WTs = 0.06 versus slope of Wfs1 deficient = 0.04, centred second order polynomial (quadratic); decline: Fig. 7 C, slope of WT = −0.007 versus Wfs1 deficient −0.004, centred second order polynomial (quadratic); peak of transient occurred at 15 s for WT cells and 17.5 s for Wfs1 deficient cells). Data from individual experiments, all of which showed the same trend, are shown in Supplemental file 1 Table S3.

With regard to mitochondria, $\Delta\Psi_M$ was significantly reduced whether measured as integrated intensity of TMRM fluorescence or mean fluorescence (Fig. 7E integrated intensity: Mann-Whitney test (F test showed variances were different) p < 0.0001, U = 27,694, WT 95 % CI 443,399–518,263, Wfs1 deficient 95 % CI 351,375–410,757; Fig. 7F mean intensity: t-test t(525) = 6.5, p < 0.0001, WT 95 % CI: 1,927–2,114, Wfs1 deficient 95 % CI: 1,451–1,661). As neurons were cultured from neonatal mice (P5-P14), these data show very early pathology in WS sensory neurons. Data per individual experiment shown in Supplementary Tables S4a and S4b (mixed-effect ANOVA for integrated intensity, effect of genotype F(1, 519) = 11.22, $p < 0.001$, mixed-effect ANOVA for mean intensity effect of genotype F(1, 519) = 37.96, p < 0.0001).

3.8. Wfs1 deficient sensory neurons show reduced lysosomal content

Given these changes in mitochondria, we next questioned whether autophagy pathways were altered in trigeminus. Although there was a tendency towards increased expression of Beclin1 and p62 in neonates, this did not reach significance and no other alterations were detected in young (P22 neonates) or old (8-month-old) Wfs1 deficient mice. The trigeminus can mediate cool or hot/itch sensations via Trpm8 or TrpA1, respectively(Kichko et al., 2018; Moore et al., 2018) but there was no alteration in these transcripts (supplementary file 1 Table S5).

Wfs1 impairment in pancreatic beta cells leads to a reduction in acidification of secretory granules(Hatanaka et al., 2011). Furthermore, reduced $\Delta\Psi_M$ and cellular ATP(Perry et al., 2011) impairs lysosome acidity(Bouhamdani et al., 2021). We therefore explored whether lysosomes were impaired in Wfs1 deficient sensory neurons. Using Lysotracker, a well-known dye that is ion-trapped in acidic environments, we found that the median lysosome volume (Fig. 8 A, Mann-Whitney test p < 0.0001; U = 7,774, WT 95 % CI 0.23–0.28, Wfs1 deficient 95 % CI 0.18–0.22) and total volume of lysosomes (thus, total content; Fig. 8 B, Mann-Whitney test $p < 0.001$; U = 8,253, WT 95 % CI 140.7–200.1, Wfs1 deficient 95 % CI 86.3–124.5) in Wfs1 deficient neurons were reduced compared with WT cells cultured in parallel. Data from individual experiments are shown in Supplementary file 1 Tables S6a and S6b (mixed-effect ANOVA for median volume, effect of genotype F (1, 284) = 11.09, $p < 0.002$; mixed-effect ANOVA for total volume, effect of genotype F (1, 284) = 12.40, p < 0.001).

Finally, we asked whether this reduction in Lysotracker staining was due to a loss in lysosomes or a change in their acidity. We co-labelled lysosomes with both Lysotracker and Lysosensor (pKa ~ 5.2). We observed a reduction in acidic organelles in DRGs from Wfs1 deficient mice compared with WT DRGs cultured in parallel (Fig. 8 C, t-test p < 0.001; $t = 3.73$, df = 414; WT 95 % CI 0.93–1.07, Wfs1 deficient 95 % CI = 0.75–0.88, effect size 0.4). Data from individual experiments are shown in Supplementary file 1 Table S6c (mixed-effect ANOVA for proportion of lysosomes that are acidic, effect of genotype F (1,120) = 6.9, $p < 0.01$). Our data suggest that primary sensory neurons from Wfs1 deficient mice may have a reduced capacity to recycle because they have

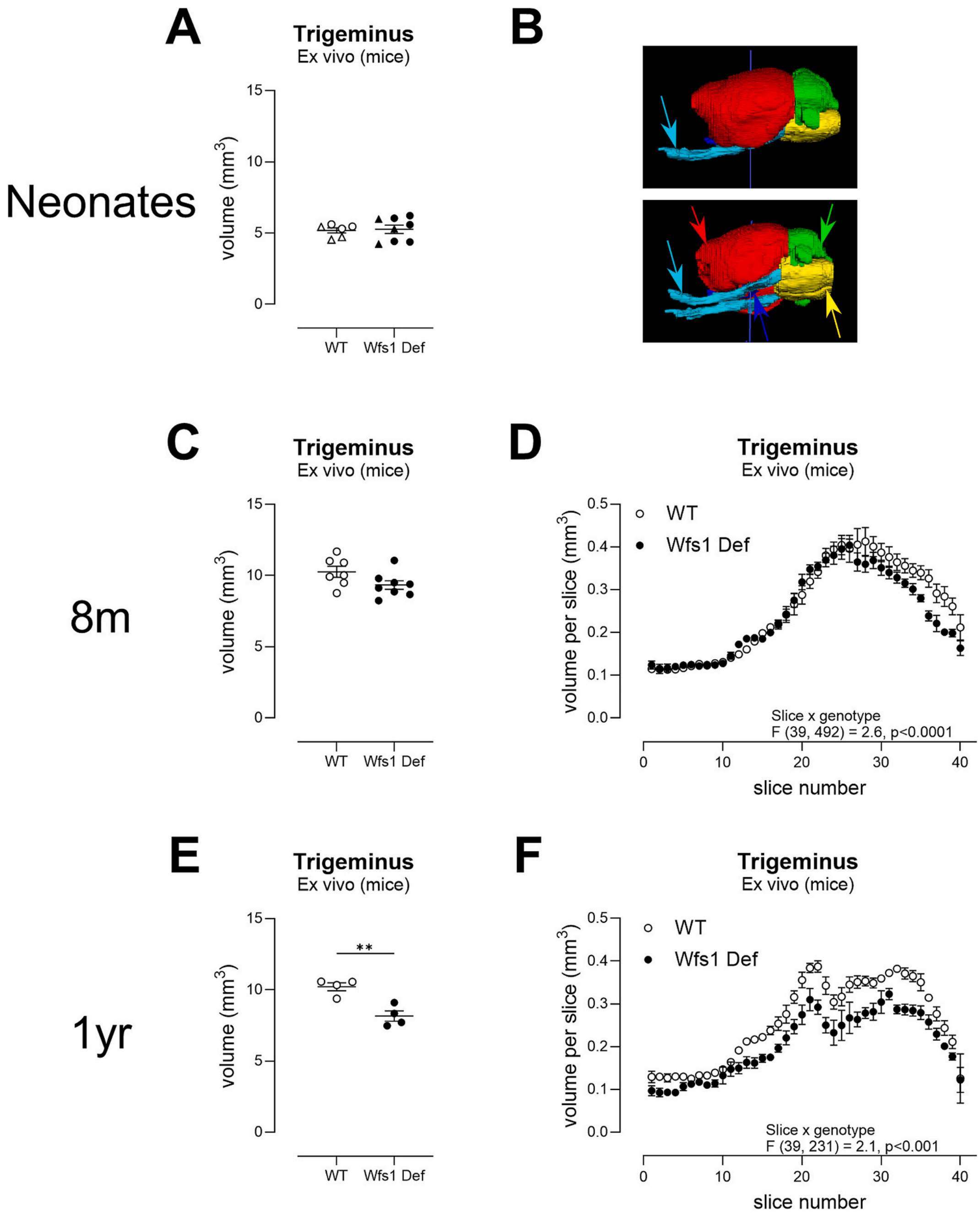

Fig. 3. Ex vivo volumetric segmentation of trigeminus (cranial nerve V) of perfusion-fixed brains from WT and Wfs1 deficient male mouse littermates. Total trigeminal volume (A, C, E) and trigeminal volume per slice (D, F). B) 3D segmentations of brain from a 1 yr-old wildtype mouse. The turquoise arrow points to trigeminus, the dark blue arrow points to the optic tract, the green arrow points to the cerebellum and the yellow arrow points to the brainstem. The overlying cerebrum is shown by the red arrow. A) Total trigeminal volume of P10 mice (shown as triangles) and P22 mice (shown as circles). C) Total trigeminal volume from 8 m-old mice. D) Trigeminal volume, per coronal slice, in 8 m-old mice. E) Total trigeminal volume in 1 yr-old mice. F) Trigeminal volume, per coronal slice, in 1 yr-old mice. **$p < 0.01$ versus WT. A, C, E, Symbols are of individual mice with group mean ± sem also shown. D, F) Symbols are of group mean ± sem. (For interpretation of the references to colour in this figure legend, the reader is referred to the web version of this article.)

reduced lysosomal load and reduced acidic lysosomes.

3.9. Reduced lysosomal content is an early feature in human WS fibroblast-derived neural stem cells

Reduced lysosomal content is a novel finding in WS. We could not conduct proteomic analyses in our samples that were used for mRNA; we therefore examined the translational impact of our findings in two recently published studies of healthy and WS patient untreated fibroblast-derived neural stem cells(Pourtoy-Brasselet et al., 2021; Zmyslowska et al., 2021).

Based upon a published library of lysosomal proteins(Schröder et al., 2010), all lysosomal matrix proteins ($N = 63$) that were expressed by neural stem cells ($N = 45$) and all lysosomal integral membrane proteins or protein complexes of the lysosome membrane ($N = 45$) that were expressed by the cells ($N = 21$) were extracted from the proteomics dataset(Zmyslowska et al., 2021). The majority of lysosomal proteins, both matrix (Fig. 9A) and integral (Fig. 9B), were reduced in WFS1 patient fibroblast-derived neural stem cells.

Separately, we conducted enrichment analyses. Proteomic data from

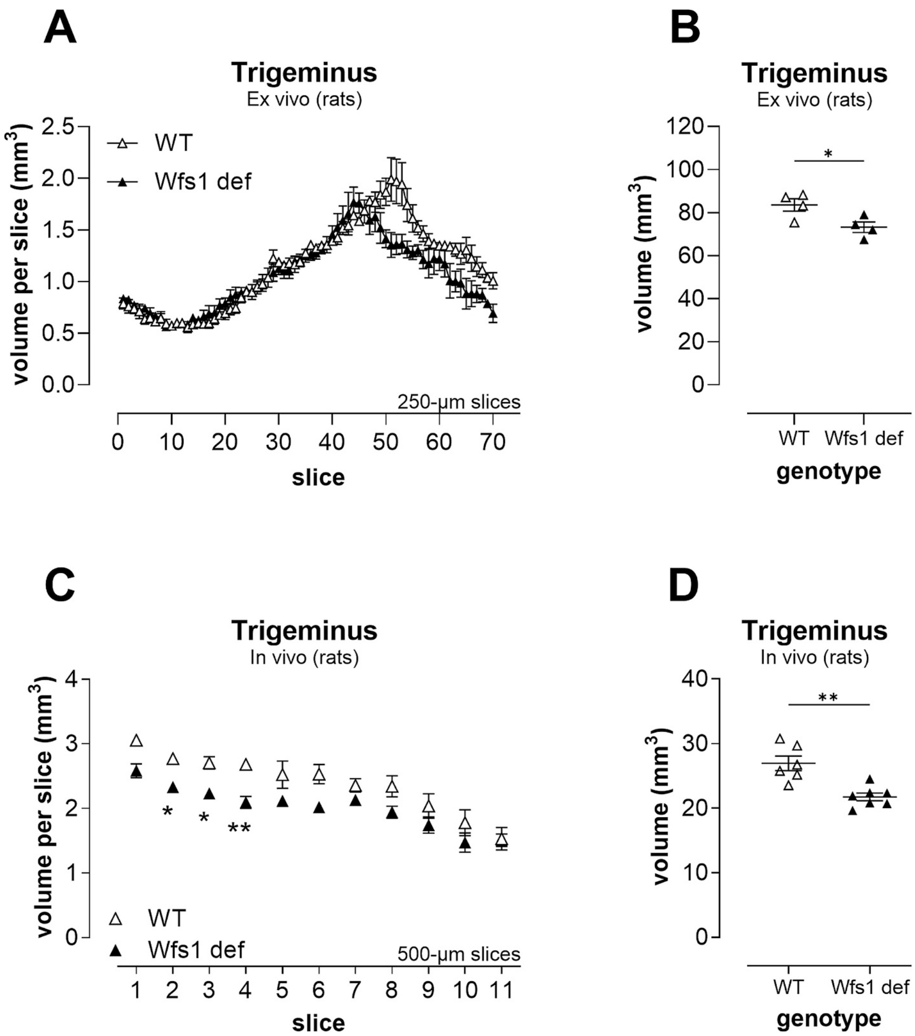

Fig. 4. Volumetric segmentation of trigeminus from WT and Wfs1 deficient male rats. Trigeminal volume per slice (A, C) or total trigeminal volume (B, D), determined ex vivo (17 months, A, B) or in vivo from live rats (15 months, C, D). Due to the reduced resolution of in vivo imaging, segmentations for in vivo sequences were from where the trigeminae erupted from foramina until bilateral contact with the pons, only (caudal trigeminus). * $p < 0.05$, **$p < 0.01$ versus WT. Symbols are of mean ± sem (A, C) or of individual mice with mean ± sem (B, D). $N = 4$–7.

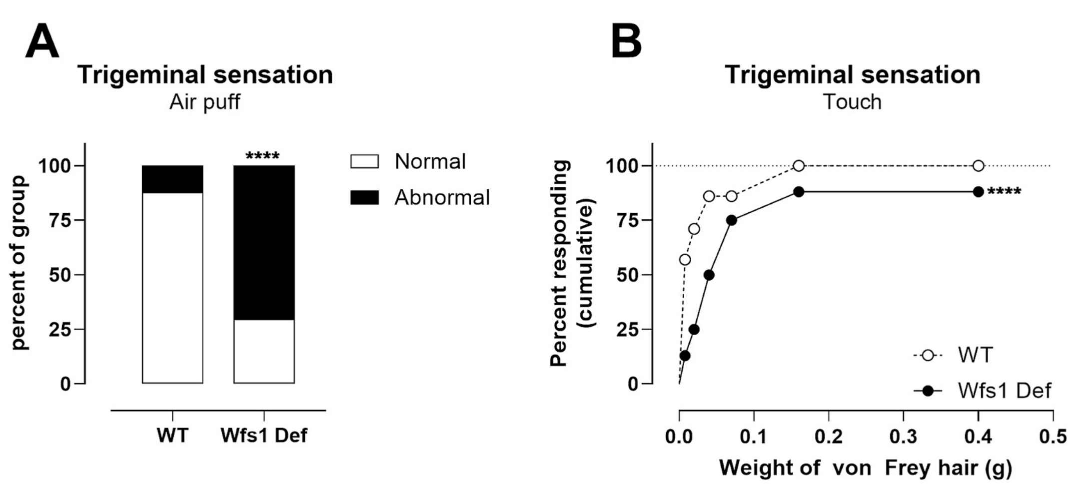

Fig. 5. Trigeminal function in 8-month-old Wfs1 deficient male mice ($N = 7$–8). A) Response to an air puff to the side of the head and directed towards the eye was abnormal in Wfs1 deficient mice (slowed, or no response). Chi-squared test, $p < 0.0001$. B) Wfs1 deficient mice required greater stimuli to respond to von Frey hairs applied to the side of the muzzle. Chi-squared test, $p < 0.0001$.

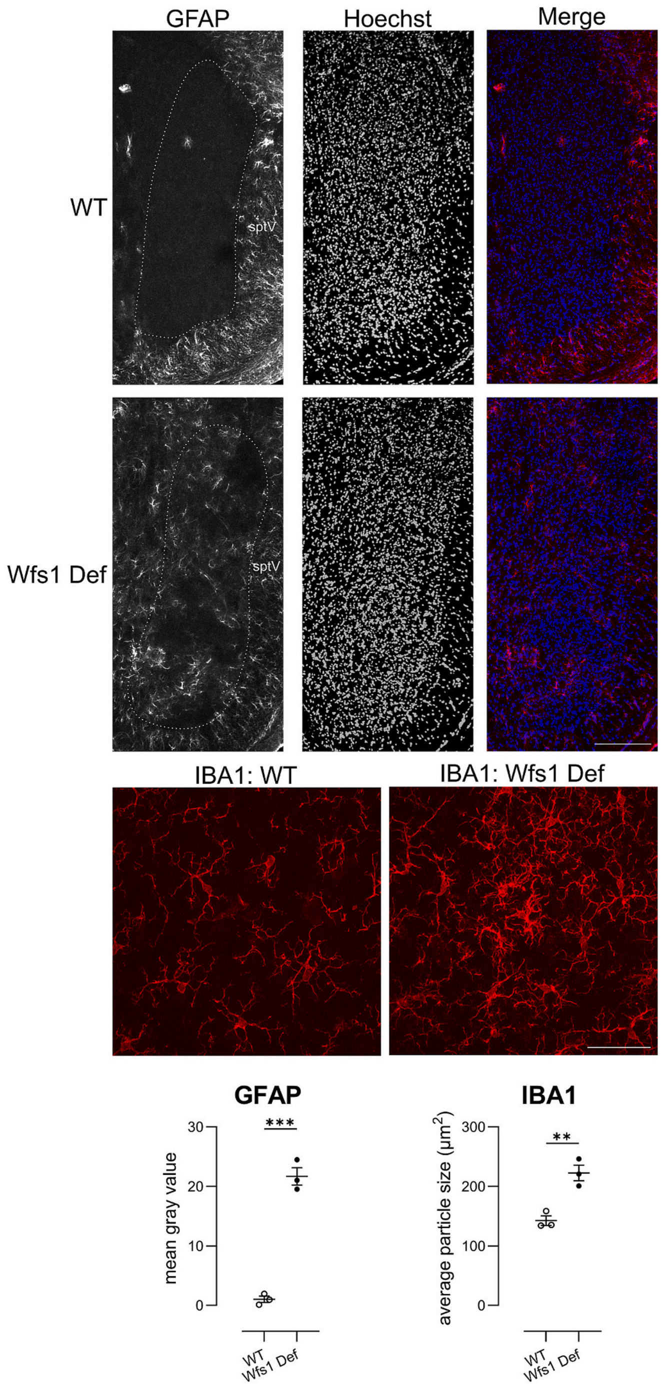

Fig. 6. Inflammation in mouse Wfs1 deficient TSN. Top two rows depict GFAP staining (left column), Hoechst-stained nuclei (middle column) and merged images (right columns) in WT (top row) and Wfs1 deficient (second row) mice. Although largely absent from TSN in WT mice, there was extensive infiltration of GFAP-positive astrocytes into the TSN in Wfs1 deficient mice. Dashed lines on GFAP images depict the TSN. IBA1 staining in mouse TSN is shown in the third row, in WT TSN (left) and Wfs1 deficient TSN (right). As expected microglia are normally present in TSN in WT mice; however, microglia are more activated in Wfs1 deficient mice, as they are larger and bushier in appearance. Graphs depict the mean gray value of GFAP staining in TSN and the mean particle size of IBA1-positive staining. $N = 3$ per genotype, mice were 8 months of age. **$p < 0.01$, ***$p < 0.001$. GFAP: glial fibrillary acidic protein; IBA1: Ionized calcium binding adaptor molecule 1; TSN, trigeminal sensory nucleus, sptV, spinal tract of the trigeminal nerve. Scalebar for GFAP images = 200 µm. Scalebar for IBA1 images = 50 µm.

the untreated healthy and WS human neural stem cells were compared, and of the 8047 proteins in the dataset, 3308 were expressed differentially (q value 0.05 or less). Enrichment analysis was then performed on these 3308 proteins using two databases, G:Profiler(Kolberg et al., 2023) and DAVID(Huang et al., 2009; Sherman et al., 2022). In G:Profiler, Gene ontology cell component (GO CC) terms primary lysosome (adjusted p value 1.90E-08, term size 154, intersection size 53, GO:0005766) and lysosome (adjusted p value 9.04E-10, term size 762, intersection size 174, GO:0005764) were highly significant with 34 % and 23 % of proteins within these GO terms enriched, respectively. In DAVID, GO CC terms lysosome and lysosomal lumen were also enriched (GO:0005764 lysosome, adjusted p value <0.003; GO:0043202 lysosomal lumen, adjusted p value $p < 0.001$).

8786 genes were published as differentially expressed (padj $p < 0.05$) in the second dataset of transcriptomics of neural stem cells derived from WS patient and control fibroblasts(Pourtoy-Brasselet et al., 2021). Examination of these DEGs again revealed enrichment of the GO CC terms lysosome (padj 2.149E-9), lysosomal membrane (1.70E-8) and lysosomal lumen (1.54E-5) in G:Profiler. These terms were also enriched when analysed using DAVID (fold: 1.3×, 1.3×, 1.7×, respectively; Benjamini-adjusted p values: $p < 0.006$, $p < 0.0006$, $p < 0.00002$). There were far fewer differentially regulated genes in the differentiated neurons derived from these cells, but the lysosome GO term was again enriched (DAVID database; 2.3-fold; Benjamini-adjusted p value $p < 0.02$).

Finally, DAVID-based analysis revealed that the KEGG(Kanehisa, 2019, 2000; Kanehisa et al., 2023) term “lysosome” was enriched in both the proteomics dataset (1.3 % of module, 1.7-fold enriched, Benjamini-adjusted p value $p < 0.01$) and the neural stem cells transcriptomics dataset (0.94 % of module, 1.5-fold enriched, Benjamini-adjusted p value $p < 0.0001$). As shown in Fig. 9C, the majority of differentially expressed proteins within the KEGG term “lysosome pathway” (04142) from the proteomics dataset(Zmyslowska et al., 2021), were downregulated (Fig. 9D, highlighted in blue), in particular lysosome acid hydrolases, although proteins involved in transport of synthesised lysosome enzymes tended to be upregulated (Fig. 9C, highlighted in red).

Thus, in two, separate, publicly available datasets of patient fibroblast-derived neural stem cells and neurons, multiple terms related to lysosomes were enriched in differentially expressed proteins and genes, which was determined using a published compendium of lysosomal proteins, in addition to two, separate, robust databases (G:Profiler and DAVID). Further exploration of the differentially expressed proteins showed that the majority of differentially expressed lysosome proteins were downregulated but lysosomal transport proteins may be upregulated. These data demonstrate that the lysosome component is greatly affected from a very early disease stage in WS.

4. Discussion

WS is a rare, incurable, genetic disorder(de Heredia et al., 2013). Increasingly, sensory deficits are being recognised in WS: patients complain of trigeminal-like pain(Urano, 2016) and show deficits in vibration sensation(Marshall et al., 2013), smell(Alfaro et al., 2023, 2020) and hearing(Serbis et al., 2023). Hearing impairments are also common in patients with Wolfram-like syndrome, a condition caused by autosomal dominant mutations in WFS1(De Muijnck et al., 2023), which may be related to the role of WFS1 in maintaining correct targeting of the beta 1 subunit of the Na^+/K^+ ATPase(Richard et al., 2023). Autosomal dominant mutations in WFS1 are also associated with cataracts (Berry et al., 2013; Krutish et al., 2023). Moreover, given that heterozygous pathogenic mutations in WFS1 are common in the general population(Aloi et al., 2012; Bespalova, 2001), mutant WFS1 may underlie sensory deficits more broadly.

We have previously shown that our WS mouse model develops the diagnostic features of WS: elevated blood glucose from 4 months of age

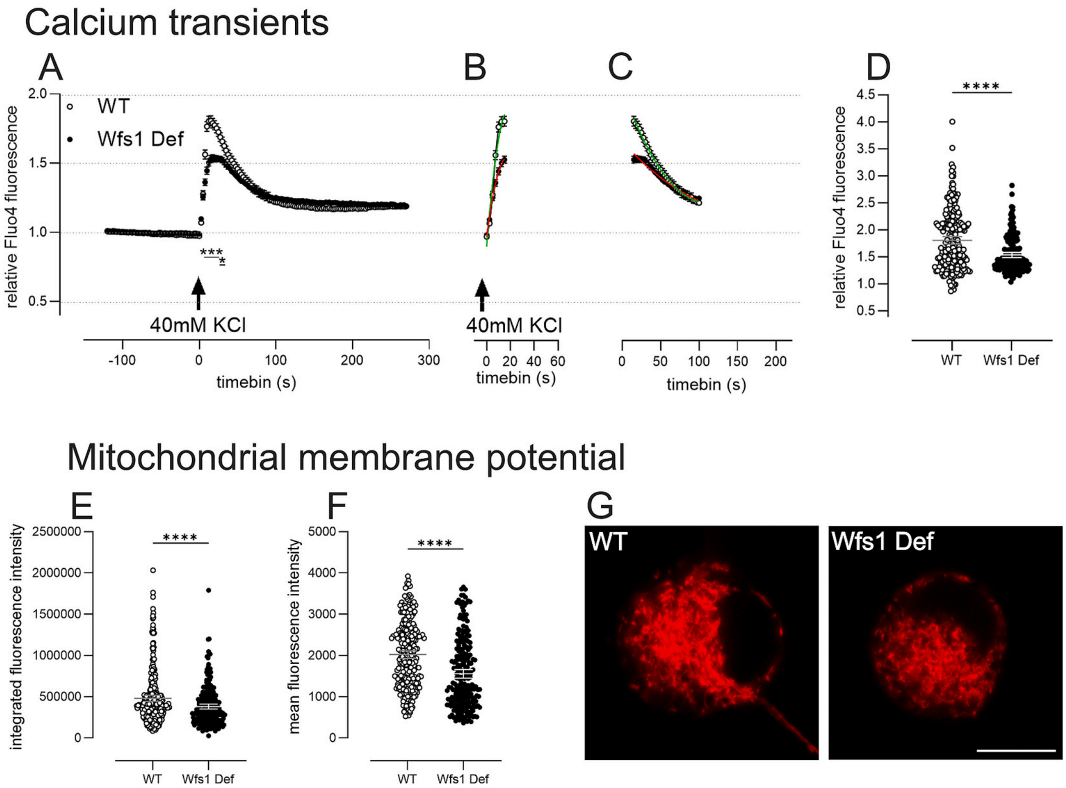

Fig. 7. Calcium transients and mitochondrial membrane potential ($\Delta\Psi_M$) in WT or Wfs1 deficient primary DRGs isolated from mixed-sex neonate mice, at 3–4 weeks DIV. A-D) Fluo-4 fluorescence intensity, relative to baseline, was quantified. As shown in A), the peak transients of Wfs1 deficient neurons in response to 40 mM KCl were smaller. In addition, both the speed of rise (B) to peak and the decline (C) from peak fluorescence were slower in Wfs1 deficient DRG soma compared with WT DRGs. Fitted curves (second order polynomial) are shown in green (WT) and red (Wfs1 deficient). AUC analysis revealed that peaks were reached at 15 s for WT soma and 17.5 s for Wfs1 deficient soma and D) peak values for Wfs1 deficient cells (at 17.5 s) were smaller than WT cells (at 15 s). N = 4 biologic replicates (experiments), always with both WT and Wfs1 deficient neurons cultured in parallel. WT $N = 234$ from 17 dishes, Wfs1 deficient $N = 177$ from 15 dishes. Symbols are of group means ± sem (A – C) or of individual soma with group mean ± 95 % CI (D). *p < 0.05, ****p < 0.0001. *E*-G) TMRM fluorescence was measured in single optical slices through the soma of DRGs. E: Integrated fluorescence intensity per soma, Mann Whitney test, p < 0.0001. F: fluorescence intensity per soma, unpaired *t*-test, **** p < 0.0001. Symbols are of individual soma and lines show mean ± 95 % CI. N = 4 biologic replicates (experiments), always with both WT and Wfs1 deficient neurons cultured in parallel. WT $N = 283$ cells from 11 quadrants, Wfs1 deficient $N = 244$ cells from 10 quadrants. G: Photomicrographs showing example WT and Wfs1 deficient DRG soma. Photomicrographs are not modified. Scalebar = 10 μm, for both photomicrographs. (For interpretation of the references to colour in this figure legend, the reader is referred to the web version of this article.)

(Luuk et al., 2009) and optic atrophy by 1 year(Cagalinec et al., 2016). Here, we extend these data. We show that at macroscopic level, brain development is normal at the very earliest stages of WS because volume measures of P10 and P22 neonate mouse brain were normal – this age is likely equivalent to human ages of between in utero and 9 months of age (Agoston, 2017; Clancy et al., 2007; Ohmura and Kuniyoshi, 2017). However, by 8 months of age, total brain volume and optic nerve volume is reduced, which are observed in children with WS(Hershey et al., 2012). Our rat model also shows elevated blood glucose, optic atrophy and loss of brainstem volume(Plaas et al., 2017) and here, we also show a loss in total brain volume. Thus, our construct- and face-valid models are ideal for examination of little-understood phenotypes that patients show.

We used these two models to gain insight into trigeminal pathology in WS. We show that Wfs1 is heavily expressed in trigeminus, and for the first time, we show reduced trigeminal mechanical sensation using two separate behavioural tests (von Frey hair and air puff), which occurred at the time of earliest detection (8-months) of trigeminal volume loss from ex vivo MRI sequences, another novel finding in WS. In keeping with the observed atrophy, axons in caudal trigeminus tended to be smaller. This atrophy worsened with age because it was initially most robust caudally but by 1 year of age, atrophy was present throughout the nerve, contributing to a loss in total volume. We replicated this pattern of atrophy in trigeminus in aged Wfs1-deficient rats imaged ex vivo and in a separate cohort imaged in vivo. Moreover, when we examined tissue from 8-month-old mice, we noted extensive inflammation in TSN, with infiltration of astrocytes and activation of microglia, which was consistent within genotypes, highly significant and showed no overlap between genotypes.

When we examined sensory neurons, we found that mature primary Wfs1 deficient DRGs showed reduced peak calcium with slowed rise in calcium and reduced speed of return following depolarisation, and reduced mitochondrial membrane potential. These deficits are reminiscent of the deficits in calcium buffering and mitochondrial impairment that we observed in primary Wfs1-deficient cortical neurons (Cagalinec et al., 2016; Liiv et al., 2024), which may reflect the critical role of WFS1 in regulating calcium via the IP3 and ryanodine receptor and SERCA(Liiv et al., 2024; Loncke et al., 2021).

There is a strong, positive effect of mitochondrial dysfunction on lysosome biogenesis(Lang et al., 2022). We examined mRNA for several autophagic genes, in trigeminal tissue taken from neonate or 8-month-old mice, thus at early stage or during symptom and sign manifestation. We did note a tendency for upregulation of Beclin1 and p62 in neonates, but this did not reach significance, and there was no change at 8 months. This suggests no global change in autophagy, despite the strong stimulating effect of mitochondrial dysfunction. Instead, we report, for the first time, a reduction in size and load of lysosomes in mature Wfs1 DRGs prepared from neonate mice. In addition, the proportion of lysosomes that were acidic was also reduced. Demonstrating the validity of our data, using data derived from two separate publicly

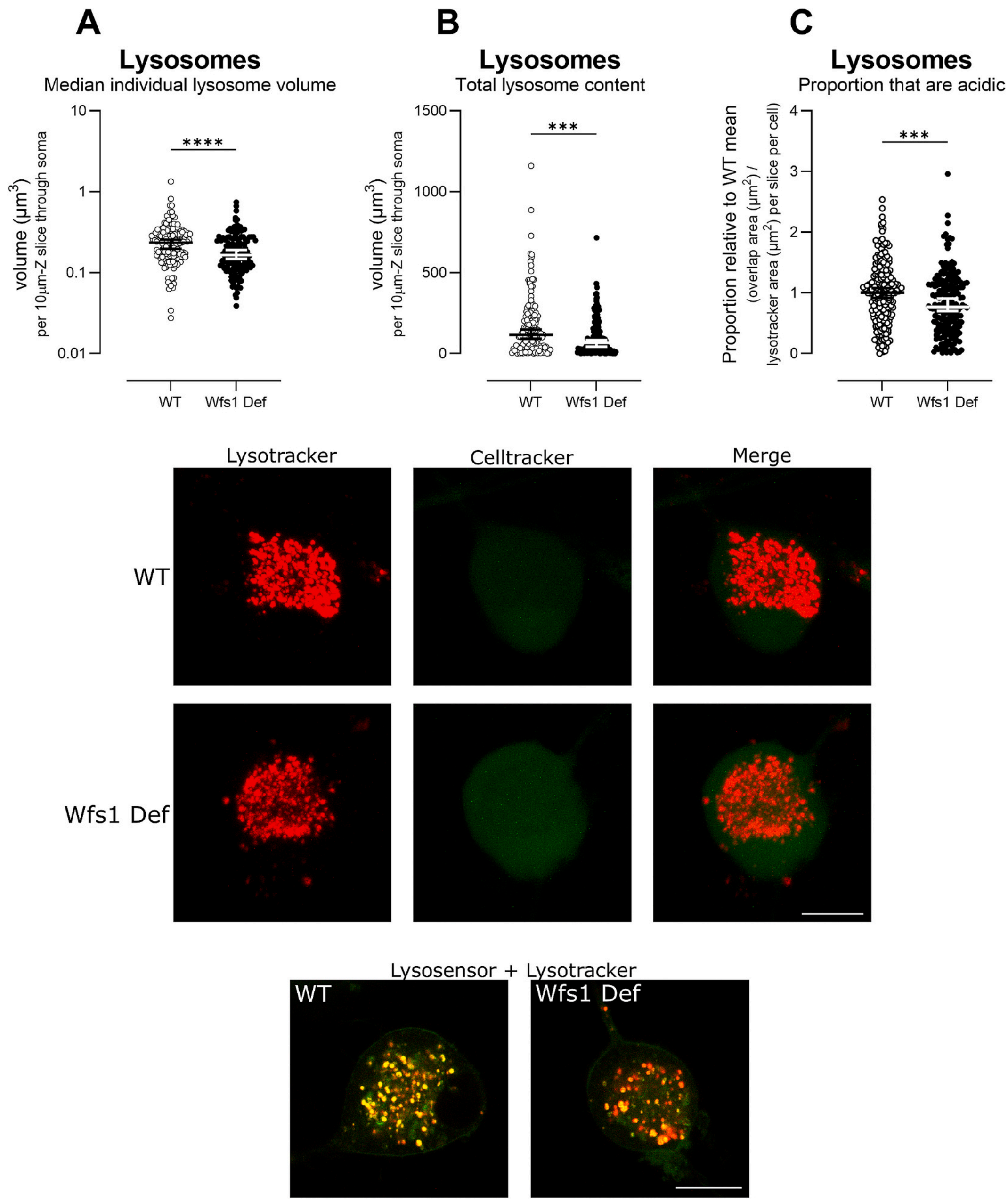

Fig. 8. Lysosomes in primary DRG soma isolated from WT or Wfs1 deficient neonatal mice, at 3–4 weeks DIV. A, B) Lysosomes were labelled using Lysotracker and soma outlined based upon CellTracker fluorescence. Lysosomes were smaller in primary DRGs from Wfs1 deficient mice (A, Mann Whitney $p < 0.0001$) and soma lysosome content was reduced (B, Mann Whitney $p < 0.001$). Photomicrographs show 3D-projections of Lysotracker-labelled lysosomes from WT mice (first row, left column) and Wfs1 deficient mice (second row, left column), with 3D-projections of soma (first and second row, middle column) together with merged images (first and second row, right column). Scalebar = 10 µm. Photomicrographs are not modified. Four separate experiments were conducted, and data were derived from N = 149 WT DRGs (14 dishes) and N = 143 Wfs1 deficient DRGs (14 dishes) in total, always with both WT and Wfs1 deficient neurons cultured in parallel and cells were grouped together for analysis. C, Wfs1 deficient lysosomes were less acidic than in DRGs from WT mice (*t*-test $p < 0.001$). Lysosomes were labelled using both Lysosensor (pKa ~5.2) and Lysotracker. Four separate experiments were conducted, and WT and Wfs1 deficient neurons were always cultured in parallel. Data from the 4 separate experiments were grouped together for analysis, N = 206 WT DRGs from 15 quadrants, N = 210 Wfs1 deficient DRGs, from 12 quadrants. Photomicrographs (third row) depict single optical planes through the soma of lysosensor- and lysotracker-labelled lysosomes. Scalebar = 10 µm for Wfs1 deficient and for WT representative somas. Photomicrographs are not modified. A, B, C: datapoints show individual soma and lines show median ± 95 % CIs.

available datasets generated from WS patient neural stem cells, one on proteomics(Zmyslowska et al., 2021) and the other on transcriptomics (Pourtoy-Brasselet et al., 2021), we also show a reduction in lysosome matrix- and integral-related proteins. There was an enrichment of lysosome-related GO CC terms (lysosome, lysosomal membrane and lysosomal lumen) in the transcriptome of neural stem cells derived from patient fibroblasts. Moreover, when we analysed the differentially expressed proteins, we observed a highly significant enrichment of the GO cellular component terms lysosome, primary lysosome and lysosomal lumen. Importantly, the KEGG "lysosome" pathway (04142) was also enriched within the proteomic dataset of differentially expressed proteins. When we examined the individual significantly dysregulated proteins within this pathway, the vast majority were again down-regulated, including several of the acid hydrolyses. However,

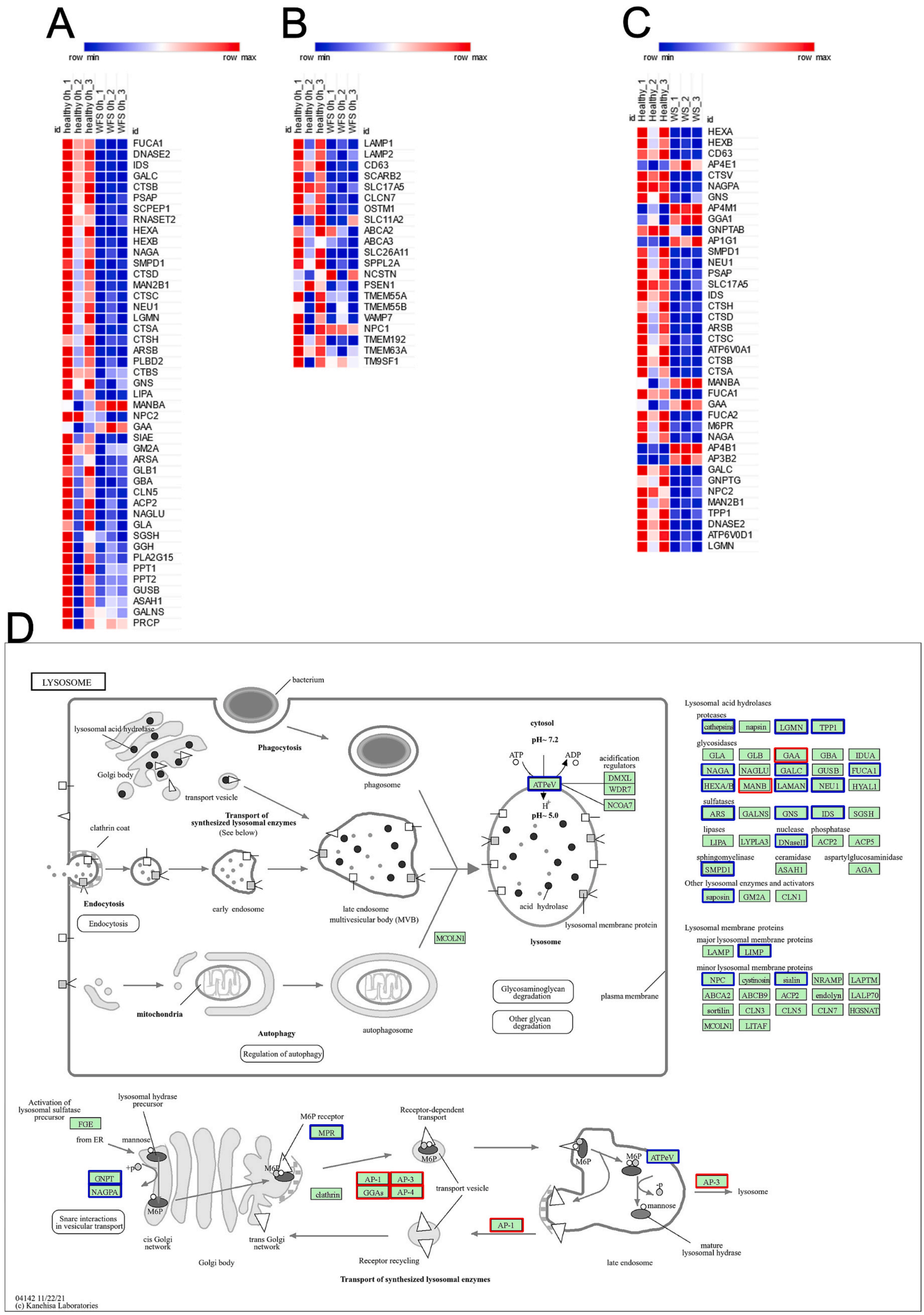

(caption on next page)

Fig. 9. Proteomics data from untreated healthy and WS patient fibroblast-derived neural stem cells were obtained from(Zmyslowska et al., 2021). Based upon a published library of lysosome proteins(Schröder et al., 2010), all lysosomal matrix proteins (*N* = 63) that were expressed by the cells (*N* = 45), and all lysosomal integral membrane proteins or protein complexes of the lysosome membrane (N = 45) that were expressed by the cells (N = 21), were extracted from the entire proteomics dataset for visual representation using Morpheus. The majority of lysosomal proteins, both matrix (A) and integral (B), show reduced expression in WS patient fibroblast-derived neural stem cells. Separately, functional enrichment analysis in DAVID(Huang et al., 2009; Sherman et al., 2022) showed that the KEGG pathway was enriched (1.3 % of module, 1.7 fold enrichment, Benjamini $p < 0.01$) and the 39 identified protein hits that were identified in this pathway were again placed in Morpheus for visual representation (C). Again, the majority of proteins downregulated (blue), although a minority are upregulated (red). D) Many of the lysosome acid hydrolases are downregulated (see blue squares) even though proteins involved in transport of lysosomal enzymes are upregulated (see red squares). Permission for use of map04142 Lysosome granted by Kanehisa Laboratories(Kanehisa, 2019, 2000; Kanehisa et al., 2023). (For interpretation of the references to colour in this figure legend, the reader is referred to the web version of this article.)

intriguingly, the proteins related to transport of synthesised lysosomal enzymes were upregulated. Lysosomal impairment is associated with several diseases, for example, variants of TMEM106B are associated with the fatal neurodegenerative disease Fronto-temporal lobar degeneration with TDP-43 (FTLD-*TDP*)(Stagi et al., 2014) and several aspects of lysosome function, including impaired biogenesis, acidification and trafficking are critical for Parkinson's disease and Alzheimer's disease pathogenesis(Nixon and Rubinsztein, 2024).

Interestingly, WFS1 stabilises the V1A subunit of the vacuolar (v) ATPase on secretory granules(Gharanei et al., 2013), and others have shown that WFS1 is required for the acidification of secretory granules in beta cells(Hatanaka et al., 2011), thus, the loss of Wfs1 may have inhibited lysosomal acidification in our primary sensory neurons – certainly, ATP6V0D1 and ATP6V0A1 were downregulated in the human neural stem cells(Zmyslowska et al., 2021) and both form part of this ATPase. Importantly, we have very recently shown that reduced mitochondrial calcium uptake from the endoplasmic reticulum in WS subsequently leads to loss of mitochondrial ATP production due to impaired Krebs recycling (Liiv et al., 2024). Energy levels are critical for correct functioning of the vATPase(Bouhamdani et al., 2021) and we and others have shown that loss of mitochondrial energy production or vATPase can lead to reduced lysosome size and lysosome acidity (De Araujo et al., 2020; Olaoye et al., 2024; Xu and Ren, 2015). Alternatively, we previously observed Wfs1-deficiency-mediated early upregulation of mitophagy(Cagalinec et al., 2016), which has been suggested to lead to reduced free lysosomes(Mutvei et al., 2023). Separately, the FTLD-*TDP* lysosomal protein TMEM106B, is reduced in WS patient neural stem cells (Zmyslowska et al., 2021), and its loss is associated with reduced lysosomal size, number and impaired lysosome response to stress (Stagi et al., 2014).

5. Conclusion

Our current data highlight a profound impairment of the trigeminal system in WS and the critical importance of Wfs1 and lysosomes for normal function of sensory neurons in WS. In the clinic, WS patients are known to complain of trigeminal neuralgia-like pain(Stone et al., 2021; Urano, 2016) and patients also show reduced vibration sensation (Marshall et al., 2013). Heterozygous mutations in WFS1 also cause sensory disturbances, such as hearing loss(De Muijnck et al., 2023; Lim et al., 2023). Moreover, given the relatively common prevalence of pathogenic WFS1 mutations in the general population(Aloi et al., 2012; Bespalova, 2001), our data may also be more broadly relevant to sensory impairments. Although relatively little transcriptomics have been conducted in trigeminal neuralgia, heredity is increasingly noted in this condition(Eide, 2022; Zorina-Lichtenwalter et al., 2018). Moreover, a polymorphism in WFS1 has previously been associated with increased analgesic drug use in patients with migraine(Di Lorenzo et al., 2007). Our data highlight a central role for Wfs1 in the trigeminal system and in peripheral nociceptive function.

Abbreviations

$\Delta\Psi_M$	mitochondrial membrane potential
DRG	dorsal root ganglia
MRI	magnetic resonance imaging
TSN	trigeminal sensory nucleus
TMN	trigeminal motor nucleus
WS	Wolfram syndrome
WT	wildtype

Funding

EEA/Iceland Liechtenstein Norway grant, under the EEA Baltic Research Cooperation Programme (36.1-2.2/680); Estonian Research Council (IUT2–5; PRG957); Horizon 2020 research and innovation programme (692202); European Regional Development Fund (Project No. 2014-2020.4.01.15-0012); Estonian-French research program Parrot. Funders had no role in the collection, analysis or interpretation of data, in the writing of this report or in the decision to submit this article for publication.

CRediT authorship contribution statement

Kerli Tulva: Writing – review & editing, Writing – original draft, Resources, Methodology, Investigation, Formal analysis, Data curation. **Aleksander Pirajev:** Writing – review & editing, Writing – original draft, Methodology, Investigation, Formal analysis, Data curation. **Akbar Zeb:** Writing – review & editing, Writing – original draft, Methodology, Investigation, Formal analysis, Data curation. **Asya E. Aksoy:** Writing – review & editing, Writing – original draft, Methodology, Investigation, Formal analysis, Data curation. **Azizah Bello:** Writing – review & editing, Writing – original draft, Methodology, Investigation, Formal analysis, Data curation. **Benjamin Lee:** Writing – review & editing, Writing – original draft, Methodology, Investigation, Formal analysis, Data curation. **Baldvin F. Guðjónsson:** Writing – review & editing, Investigation, Formal analysis, Data curation. **Sigridur B. Helgadottir:** Writing – review & editing, Investigation, Formal analysis. **Toomas Jagomäe:** Writing – review & editing, Resources. **Andrea García-Llorca:** Writing – review & editing, Supervision. **Thor Eysteinsson:** Writing – review & editing, Supervision, Funding acquisition. **Monika Jürgenson:** Writing – review & editing, Supervision, Funding acquisition. **Mario Plaas:** Writing – review & editing, Resources, Methodology, Funding acquisition. **Eero Vasar:** Writing – review & editing, Resources, Methodology. **Allen Kaasik:** Writing – review & editing, Supervision, Resources, Project administration, Methodology, Funding acquisition, Conceptualization. **Miriam A. Hickey:** Writing – review & editing, Writing – original draft, Visualization, Supervision, Resources, Project administration, Methodology, Investigation, Funding acquisition, Formal analysis, Data curation, Conceptualization.

Declaration of competing interest

The authors declare no conflicts of interest.

Data availability

Data available within https://doi.org/10.23673/re-495

Acknowledgements

We thank Ruth Pooga for expert assistance with genotyping, Ulla Peterson for excellent assistance with primary cultures and Oili Suvi for excellent assistance with mice and tissue processing. We thank Dr. Indrek Heinla for assistance with MR imaging. We thank Mait Nigul, medical physicist, for developing our MRI sequences.

Appendix A. Supplementary data

Supplementary data to this article can be found online at https://doi.org/10.1016/j.expneurol.2024.115099.

References

Agoston, D.V., 2017. How to translate time? The temporal aspect of human and rodent biology. Front. Neurol. 8. https://doi.org/10.3389/fneur.2017.00092.

Alfaro, R., Doty, T., Narayanan, A., Lugar, H., Hershey, T., Pepino, M.Y., 2020. Taste and smell function in Wolfram syndrome. Orphanet J. Rare Dis. 15, 57. https://doi.org/10.1186/s13023-020-1335-7.

Alfaro, R., Nicanor-Carreón, J.G., Doty, T., Lugar, H., Hershey, T., Pepino, M.Y., 2023. Enhancement of taste by retronasal odors in patients with Wolfram syndrome and decreased olfactory function. Chem. Senses 48, bjad004. https://doi.org/10.1093/chemse/bjad004.

Aloi, C., Salina, A., Pasquali, L., Lugani, F., Perri, K., Russo, C., Tallone, R., Ghiggeri, G. M., Lorini, R., d'Annunzio, G., 2012. Wolfram syndrome: new mutations, different phenotype. PLoS One 7, e29150. https://doi.org/10.1371/journal.pone.0029150.

Berry, V., Gregory-Evans, C., Emmett, W., Waseem, N., Raby, J., Prescott, D., Moore, A. T., Bhattacharya, S.S., 2013. Wolfram gene (WFS1) mutation causes autosomal dominant congenital nuclear cataract in humans. Eur. J. Hum. Genet. 21, 1356–1360.

Bespalova, I.N., 2001. Mutations in the Wolfram syndrome 1 gene (WFS1) are a common cause of low frequency sensorineural hearing loss. Hum. Mol. Genet. 10, 2501–2508. https://doi.org/10.1093/hmg/10.22.2501.

Bouhamdani, N., Comeau, D., Turcotte, S., 2021. A compendium of information on the lysosome. Front. Cell Dev. Biol. 9, 798262. https://doi.org/10.3389/fcell.2021.798262.

Bustin, S.A., Benes, V., Garson, J.A., Hellemans, J., Huggett, J., Kubista, M., Mueller, R., Nolan, T., Pfaffl, M.W., Shipley, G.L., Vandesompele, J., Wittwer, C.T., 2009. The MIQE guidelines: minimum information for publication of quantitative real-time PCR experiments. Clin. Chem. 55, 611–622. https://doi.org/10.1373/clinchem.2008.112797.

Cagalinec, M., Liiv, M., Hodurova, Z., Hickey, M.A., Vaarmann, A., Mandel, M., Zeb, A., Choubey, V., Kuum, M., Safiulina, D., Vasar, E., Veksler, V., Kaasik, A., 2016. Role of mitochondrial dynamics in neuronal development: mechanism for Wolfram syndrome. PLoS Biol. 14, e1002511. https://doi.org/10.1371/journal.pbio.1002511.

Clancy, B., Kersh, B., Hyde, J., Darlington, R.B., Anand, K.J.S., Finlay, B.L., 2007. Web-based method for translating neurodevelopment from laboratory species to humans. Neuroinformatics 5, 79–94. https://doi.org/10.1385/NI:5:1:79.

Connolly, N.M.C., Theurey, P., Adam-Vizi, V., Bazan, N.G., Bernardi, P., Bolaños, J.P., Culmsee, C., Dawson, V.L., Deshmukh, M., Duchen, M.R., Düssmann, H., Fiskum, G., Galindo, M.F., Hardingham, G.E., Hardwick, J.M., Jekabsons, M.B., Jonas, E.A., Jordán, J., Lipton, S.A., Manfredi, G., Mattson, M.P., McLaughlin, B., Methner, A., Murphy, A.N., Murphy, M.P., Nicholls, D.G., Polster, B.M., Pozzan, T., Rizzuto, R., Satrústegui, J., Slack, R.S., Swanson, R.A., Swerdlow, R.H., Will, Y., Ying, Z., Joselin, A., Gioran, A., Moreira Pinho, C., Watters, O., Salvucci, M., Llorente-Folch, I., Park, D.S., Bano, D., Ankarcrona, M., Pizzo, P., Prehn, J.H.M., 2018. Guidelines on experimental methods to assess mitochondrial dysfunction in cellular models of neurodegenerative diseases. Cell Death Differ. 25, 542–572. https://doi.org/10.1038/s41418-017-0020-4.

De Araujo, M.E.G., Liebscher, G., Hess, M.W., Huber, L.A., 2020. Lysosomal size matters. Traffic 21, 60–75. https://doi.org/10.1111/tra.12714.

De Muijnck, C., Brink, J.B.T., Bergen, A.A., Boon, C.J.F., Van Genderen, M.M., 2023. Delineating Wolfram-like syndrome: a systematic review and discussion of the WFS1-associated disease spectrum. Surv. Ophthalmol. 68, 641–654. https://doi.org/10.1016/j.survophthal.2023.01.012.

Di Lorenzo, C., Sances, G., Di Lorenzo, G., Rengo, C., Ghiotto, N., Guaschino, E., Perrotta, A., Santorelli, F.M., Grieco, G.S., Troisi, A., Siracusano, A., Pierelli, F., Nappi, G., Casali, C., 2007. The wolframin His611Arg polymorphism influences medication overuse headache. Neurosci. Lett. 424, 179–184. https://doi.org/10.1016/j.neulet.2007.07.037.

Dziak, J.J., Dierker, L.C., Abar, B., 2020. The interpretation of statistical power after the data have been gathered. Curr. Psychol. 39, 870–877. https://doi.org/10.1007/s12144-018-0018-1.

Eide, P.K., 2022. Familial occurrence of classical and idiopathic trigeminal neuralgia. J. Neurol. Sci. 434, 120101. https://doi.org/10.1016/j.jns.2021.120101.

Faisal, M., Aid, J., Nodirov, B., Lee, B., Hickey, M.A., 2023. Preclinical trials in Alzheimer's disease: sample size and effect size for behavioural and neuropathological outcomes in 5xFAD mice. PLoS One 18, e0281003. https://doi.org/10.1371/journal.pone.0281003.

Faisal, M., Rusetskaya, A., Väli, L., Taba, P., Minajeva, A., Hickey, M.A., 2024. No evidence of sensory neuropathy in a traditional mouse model of idiopathic Parkinson's disease. Cells 13, 799. https://doi.org/10.3390/cells13100799.

Fernández-Montoya, J., Avendaño, C., Negredo, P., 2017. The glutamatergic system in primary somatosensory neurons and its involvement in sensory input-dependent plasticity. Int. J. Mol. Sci. 19, 69. https://doi.org/10.3390/ijms19010069.

Gharanei, S., Zatyka, M., Astuti, D., Fenton, J., Sik, A., Nagy, Z., Barrett, T.G., 2013. Vacuolar-type H+-ATPase V1A subunit is a molecular partner of Wolfram syndrome 1 (WFS1) protein, which regulates its expression and stability. Hum. Mol. Genet. 22, 203–217. https://doi.org/10.1093/hmg/dds400.

Greenland, S., Senn, S.J., Rothman, K.J., Carlin, J.B., Poole, C., Goodman, S.N., Altman, D.G., 2016. Statistical tests, P values, confidence intervals, and power: a guide to misinterpretations. Eur. J. Epidemiol. 31, 337–350. https://doi.org/10.1007/s10654-016-0149-3.

Hatanaka, M., Tanabe, K., Yanai, A., Ohta, Y., Kondo, M., Akiyama, M., Shinoda, K., Oka, Y., Tanizawa, Y., 2011. Wolfram syndrome 1 gene (WFS1) product localizes to secretory granules and determines granule acidification in pancreatic -cells. Hum. Mol. Genet. 20, 1274–1284. https://doi.org/10.1093/hmg/ddq568.

Heckman, M.G., Davis, J.M., Crowson, C.S., 2022. Post hoc power calculations: an inappropriate method for interpreting the findings of a research study. J. Rheumatol. 49, 867–870. https://doi.org/10.3899/jrheum.211115.

de Heredia, M.L., Clèries, R., Nunes, V., 2013. Genotypic classification of patients with Wolfram syndrome: insights into the natural history of the disease and correlation with phenotype. Genet. Med. 15, 497–506. https://doi.org/10.1038/gim.2012.180.

Hershey, T., Lugar, H.M., Shimony, J.S., Rutlin, J., Koller, J.M., Perantie, D.C., Paciorkowski, A.R., Eisenstein, S.A., Permutt, M.A., Group, the W.U.W.S, 2012. Early brain vulnerability in Wolfram syndrome. PLoS One 7, e40604. https://doi.org/10.1371/journal.pone.0040604.

Hickey, M.A., Gallant, K., Gross, G.G., Levine, M.S., Chesselet, M.-F., 2005. Early behavioral deficits in R6/2 mice suitable for use in preclinical drug testing. Neurobiol. Dis. 20. https://doi.org/10.1016/j.nbd.2005.01.024.

Hickey, M.A., Kosmalska, A., Enayati, J., Cohen, R., Zeitlin, S., Levine, M.S., Chesselet, M.-F., 2008. Extensive early motor and non-motor behavioral deficits are followed by striatal neuronal loss in knock-in Huntington's disease mice. Neuroscience 157. https://doi.org/10.1016/j.neuroscience.2008.08.041.

Hu, K., Zatyka, M., Astuti, D., Beer, N., Dias, R.P., Kulkarni, A., Ainsworth, J., Wright, B., Majander, A., Yu-Wai-Man, P., Williams, D., Barrett, T., 2022. WFS1 protein expression correlates with clinical progression of optic atrophy in patients with Wolfram syndrome. J. Med. Genet. 59, 65–74. https://doi.org/10.1136/jmedgenet-2020-107257.

Huang, D.W., Sherman, B.T., Lempicki, R.A., 2009. Systematic and integrative analysis of large gene lists using DAVID bioinformatics resources. Nat. Protoc. 4, 44–57. https://doi.org/10.1038/nprot.2008.211.

Kanehisa, M., 2000. KEGG: Kyoto encyclopedia of genes and genomes. Nucleic Acids Res. 28, 27–30. https://doi.org/10.1093/nar/28.1.27.

Kanehisa, M., 2019. Toward understanding the origin and evolution of cellular organisms. Protein Sci. 28, 1947–1951. https://doi.org/10.1002/pro.3715.

Kanehisa, M., Furumichi, M., Sato, Y., Kawashima, M., Ishiguro-Watanabe, M., 2023. KEGG for taxonomy-based analysis of pathways and genomes. Nucleic Acids Res. 51, D587–D592. https://doi.org/10.1093/nar/gkac963.

Kichko, T.I., Neuhuber, W., Kobal, G., Reeh, P.W., 2018. The roles of TRPV1, TRPA1 and TRPM8 channels in chemical and thermal sensitivity of the mouse oral mucosa. Eur. J. Neurosci. 47, 201–210. https://doi.org/10.1111/ejn.13799.

Kolberg, L., Raudvere, U., Kuzmin, I., Adler, P., Vilo, J., Peterson, H., 2023. G: profiler—interoperable web service for functional enrichment analysis and gene identifier mapping (2023 update). Nucleic Acids Res. 51, W207–W212. https://doi.org/10.1093/nar/gkad347.

Kreidler, S.M., Muller, K.E., Grunwald, G.K., Ringham, B.M., Coker-Dukowitz, Z., Sakhadeo, U.R., Baron, A.E., Glueck, D.H., 2013. GLIMMPSE : online power computation for linear models with and without a baseline covariate. J. Stat. Softw. 54. https://doi.org/10.18637/jss.v054.i10.

Krutish, A., Elmore, J., Ilse, W., Johnston, J.L., Hittel, D., Kerr, M., Khan, A., Rockman-Greenberg, C., Mhanni, A.A., on behalf of the Canadian Prairie Metabolic Network (CPMN), 2023. A novel *WFS1* variant associated with isolated congenital cataracts. Mol. Case Stud. 9, a006259. https://doi.org/10.1101/mcs.a006259.

Krzyzanowska, A., Pittolo, S., Cabrerizo, M., Sánchez-López, J., Krishnasamy, S., Venero, C., Avendaño, C., 2011. Assessing nociceptive sensitivity in mouse models of inflammatory and neuropathic trigeminal pain. J. Neurosci. Methods 201, 46–54. https://doi.org/10.1016/j.jneumeth.2011.07.006.

Lang, M., Pramstaller, P.P., Pichler, I., 2022. Crosstalk of organelles in Parkinson's disease – MiT family transcription factors as central players in signaling pathways connecting mitochondria and lysosomes. Mol. Neurodegener. 17, 50. https://doi.org/10.1186/s13024-022-00555-7.

Lee, K., Kim, J., Park, Y.A., Park, Y.G., Lee, W., Son, E., 2011. Evaluation of trigeminal nerve involvement using blink reflex test in Bell's palsy. Korean J. Audiol. 15, 129–132.

Liiv, M., Vaarmann, A., Safiulina, D., Choubey, V., Gupta, R., Kuum, M., Janickova, L., Hodurova, Z., Cagalinec, M., Zeb, A., Hickey, M.A., Huang, Y.-L., Gogichaishvili, N., Mandel, M., Plaas, M., Vasar, E., Loncke, J., Vervliet, T., Tsai, T.-F., Bultynck, G., Veksler, V., Kaasik, A., 2024. ER calcium depletion as a key driver for impaired ER-

to-mitochondria calcium transfer and mitochondrial dysfunction in Wolfram syndrome. Nat. Commun. 15, 6143. https://doi.org/10.1038/s41467-024-50502-x.
Lim, H.D., Lee, S.M., Yun, Y.J., Lee, D.H., Lee, J.H., Oh, S.-H., Lee, S.-Y., 2023. WFS1 autosomal dominant variants linked with hearing loss: update on structural analysis and cochlear implant outcome. BMC Med. Genet. 16, 79. https://doi.org/10.1186/s12920-023-01506-x.
Loncke, J., Vervliet, T., Parys, J.B., Kaasik, A., Bultynck, G., 2021. Uniting the divergent Wolfram syndrome–linked proteins WFS1 and CISD2 as modulators of ca 2+ signaling. Sci. Signal. 14. https://doi.org/10.1126/scisignal.abc6165.
Lugar, H.M., Koller, J.M., Rutlin, J., Eisenstein, S.A., Neyman, O., Narayanan, A., Chen, L., Shimony, J.S., Hershey, T., 2019. Evidence for altered neurodevelopment and neurodegeneration in Wolfram syndrome using longitudinal morphometry. Sci. Rep. 9, 6010. https://doi.org/10.1038/s41598-019-42447-9.
Luuk, H., Koks, S., Plaas, M., Hannibal, J., Rehfeld, J.E.V., 2008. Distribution of Wfs1 protein in the central nervous system of the mouse and its relation to clinical symptoms of the Wolfram syndrome. J. Comp. Neurol. 509, 642–660.
Luuk, H., Plaas, M., Raud, S., Innos, J., Sütt, S., Lasner, H., Abramov, U., Kurrikoff, K., Kõks, S., Vasar, E., 2009. Wfs1-deficient mice display impaired behavioural adaptation in stressful environment. Behav. Brain Res. 198, 334–345.
Marshall, B.A., Permutt, M.A., Paciorkowski, A.R., Hoekel, J., Karzon, R., Wasson, J., Viehover, A., White, N.H., Shimony, J.S., Manwaring, L., Austin, P., Hullar, T.E., Hershey, T., the Washington University Wolfram Study Group, 2013. Phenotypic characteristics of early Wolfram syndrome. Orphanet J. Rare Dis. 8, 64. https://doi.org/10.1186/1750-1172-8-64.
Moore, C., Gupta, R., Jordt, S.-E., Chen, Y., Liedtke, W.B., 2018. Regulation of pain and itch by TRP channels. Neurosci. Bull. 34, 120–142. https://doi.org/10.1007/s12264-017-0200-8.
Mutvei, A.P., Nagiec, M.J., Blenis, J., 2023. Balancing lysosome abundance in health and disease. Nat. Cell Biol. 25, 1254–1264. https://doi.org/10.1038/s41556-023-01197-7.
Nixon, R.A., Rubinsztein, D.C., 2024. Mechanisms of autophagy–lysosome dysfunction in neurodegenerative diseases. Nat. Rev. Mol. Cell Biol. 25, 926–946. https://doi.org/10.1038/s41580-024-00757-5.
Ohmura, Y., Kuniyoshi, Y., 2017. A translational model to determine rodent's age from human foetal age. Sci. Rep. 7, 17248. https://doi.org/10.1038/s41598-017-17571-z.
Olaoye, O.J., Aksoy, A.E., Hyytiäinen, S.V., Narits, A.A., Hickey, M.A., 2024. Levodopa impairs lysosomal function in sensory neurons in vitro. Biology 13, 893. https://doi.org/10.3390/biology13110893.
Percie du Sert, N., Ahluwalia, A., Alam, S., Avey, M.T., Baker, M., Browne, W.J., Clark, A., Cuthill, I.C., Dirnagl, U., Emerson, M., Garner, P., Holgate, S.T., Howells, D.W., Hurst, V., Karp, N.A., Lazic, S.E., Lidster, K., MacCallum, C.J., Macleod, M., Pearl, E.J., Petersen, O.H., Rawle, F., Reynolds, P., Rooney, K., Sena, E. S., Silberberg, S.D., Steckler, T., Würbel, H., 2020. Reporting animal research: explanation and elaboration for the ARRIVE guidelines 2.0. PLoS Biol. 18, e3000411. https://doi.org/10.1371/journal.pbio.3000411.
Perry, S.W., Norman, J.P., Barbieri, J., Brown, E.B., Gelbard, H.A., 2011. Mitochondrial membrane potential probes and the proton gradient: a practical usage guide. BioTechniques 50, 98–115. https://doi.org/10.2144/000113610.
Philbrook, C., Fritz, E., Weiher, H., 2005. Expressional and functional studies of Wolframin, the gene function deficient in Wolfram syndrome, in mice and patient cells. Exp. Gerontol. 40, 671–678. https://doi.org/10.1016/j.exger.2005.06.008.
Plaas, M., Seppa, K., Reimets, R., Jagomäe, T., Toots, M., Koppel, T., Vallisoo, T., Nigul, M., Heinla, I., Meier, R., Kaasik, A., Piirsoo, A., Hickey, M.A., Terasmaa, A., Vasar, E., 2017. Wfs1-deficient rats develop primary symptoms of Wolfram syndrome: insulin-dependent diabetes, optic nerve atrophy and medullary degeneration. Sci. Rep. 7. https://doi.org/10.1038/s41598-017-09392-x.
Pourtoy-Brasselet, S., Sciauvaud, A., Boza-Moran, M.-G., Cailleret, M., Jarrige, M., Polvèche, H., Polentes, J., Chevet, E., Martinat, C., Peschanski, M., Aubry, L., 2021. Human iPSC-derived neurons reveal early developmental alteration of neurite outgrowth in the late-occurring neurodegenerative Wolfram syndrome. Am. J. Hum. Genet. 108, 2171–2185. https://doi.org/10.1016/j.ajhg.2021.10.001.
Richard, E.M., Brun, E., Korchagina, J., Crouzier, L., Affortit, C., Alves, S., Cazevieille, C., Mausset-Bonnefont, A.-L., Lenoir, M., Puel, J.-L., Maurice, T., Thiry, M., Wang, J., Delprat, B., 2023. Wfs1E864K knock-in mice illuminate the fundamental role of Wfs1 in endocochlear potential production. Cell Death Dis. 14, 387. https://doi.org/10.1038/s41419-023-05912-y.
Rigoli, L., Caruso, V., Salzano, G., Lombardo, F., 2022. Wolfram syndrome 1: from genetics to therapy. Int. J. Environ. Res. Public Health 19. https://doi.org/10.3390/ijerph19063225.
Schmittgen, T.D., Livak, K.J., 2008. Analyzing real-time PCR data by the comparative CT method. Nat. Protoc. 3. https://doi.org/10.1038/nprot.2008.73.
Schröder, B.A., Wrocklage, C., Hasilik, A., Saftig, P., 2010. The proteome of lysosomes. PROTEOMICS 10, 4053–4076. https://doi.org/10.1002/pmic.201000196.
Serbis, A., Rallis, D., Giapros, V., Galli-Tsinopoulou, A., Siomou, E., 2023. Wolfram syndrome 1: a pediatrician's and pediatric endocrinologist's perspective. Int. J. Mol. Sci. 24, 3690. https://doi.org/10.3390/ijms24043690.
du Sert, N.P., Hurst, V., Ahluwalia, A., Alam, S., Avey, M.T., Baker, M., Browne, W.J., Clark, A., Cuthill, I.C., Dirnagl, U., Emerson, M., Garner, P., Holgate, S.T., Howells, D.W., Karp, N.A., Lazic, S.E., Lidster, K., MacCallum, C.J., Macleod, M., Pearl, E.J., Petersen, O.H., Rawle, F., Reynolds, P., Rooney, K., Sena, E.S., Silberberg, S.D., Steckler, T., Würbel, H., 2020. The arrive guidelines 2.0: updated guidelines for reporting animal research. PLoS Biol. 18, 1–12. https://doi.org/10.1371/journal.pbio.3000410.
Sherman, B.T., Hao, M., Qiu, J., Jiao, X., Baseler, M.W., Lane, H.C., Imamichi, T., Chang, W., 2022. DAVID: a web server for functional enrichment analysis and functional annotation of gene lists (2021 update). Nucleic Acids Res. 50, W216–W221. https://doi.org/10.1093/nar/gkac194.
Stagi, M., Klein, Z.A., Gould, T.J., Bewersdorf, J., Strittmatter, S.M., 2014. Lysosome size, motility and stress response regulated by fronto-temporal dementia modifier TMEM106B. Mol. Cell. Neurosci. 61, 226–240. https://doi.org/10.1016/j.mcn.2014.07.006.
Standring, S., 2008. Gray's anatomy. Elsevier.
Stone, S.I., Abreu, D., McGill, J.B., Urano, F., 2021. Monogenic and syndromic diabetes due to endoplasmic reticulum stress. J. Diabetes Complicat. 35, 107618. https://doi.org/10.1016/j.jdiacomp.2020.107618.
Urano, F., 2016. Wolfram syndrome: diagnosis, management, and treatment. Curr. Diab. Rep. 16, 6. https://doi.org/10.1007/s11892-015-0702-6.
Vermeiren, S., Bellefroid, E.J., Desiderio, S., 2020. Vertebrate sensory ganglia: common and divergent features of the transcriptional programs generating their functional specialization. Front. Cell Dev. Biol. 8. https://doi.org/10.3389/fcell.2020.587699.
Willner, P., 1984. The validity of animal models of depression. Psychopharmacology 83, 1–16. https://doi.org/10.1007/BF00427414.
Xu, H., Ren, D., 2015. Lysosomal physiology. Annu. Rev. Physiol. 77, 57–80. https://doi.org/10.1146/annurev-physiol-021014-071649.
Zmyslowska, A., Fendler, W., Waszczykowska, A., Niwald, A., Borowiec, M., Jurowski, P., Mlynarski, W., 2017. Retinal thickness as a marker of disease progression in longitudinal observation of patients with Wolfram syndrome. Acta Diabetol. 54, 1019–1024. https://doi.org/10.1007/s00592-017-1042-6.
Zmyslowska, A., Kuljanin, M., Malachowska, B., Stanczak, M., Michalek, D., Wlodarczyk, A., Grot, D., Taha, J., Pawlik, B., Lebiedzińska-Arciszewska, M., Nieznanska, H., Wieckowski, M.R., Rieske, P., Mancias, J.D., Borowiec, M., Mlynarski, W., Fendler, W., 2021. Multiomic analysis on human cell model of wolfram syndrome reveals changes in mitochondrial morphology and function. Cell Commun. Sign. 19, 116. https://doi.org/10.1186/s12964-021-00791-2.
Zorina-Lichtenwalter, K., Parisien, M., Diatchenko, L., 2018. Genetic studies of human neuropathic pain conditions: a review. Pain 159, 583–594. https://doi.org/10.1097/j.pain.0000000000001099.